Pixel-less And Pixel-lated Inorganic/Organic Hybrid Infrared Imaging Upconversion Devices

by

Jianchen Tao

A thesis
presented to the University of Waterloo
in fulfillment of the
thesis requirement for the degree of
Master of Applied Science
in
Electrical and Computer Engineering

Waterloo, Ontario, Canada, 2012

© Jianchen Tao 2012

I hereby declare that I am the sole author of this thesis. This is a true copy of the thesis, including any required final revisions, as accepted by my examiners.

I understand that my thesis may be made electronically available to the public.

Abstract

Nowadays, the industrial standard for infrared imaging systems is to interconnect an infrared photodetector array with a silicon-based read-out-integrated circuit pixel by pixel through existing indium bumping technology for infrared scene detection and then the signal is output optically through a LCD or other imaging devices. Motivated by the high-cost and low-resolution of such configurations, technology that up-converts infrared light to visible light and in particular, an inorganic/organic hybrid imaging upconverter has been developed. The end goal was to provide a high-efficiency and high-resolution alternative for infrared imaging. The inorganic/organic hybrid architecture takes advantage of both the high quantum efficiency of photo-detection for inorganic semiconductors, and the low-cost processing and the topologically perfect structure of organic semiconductors that does not require lattice matching for materials. Based on previous single-element hybrid infrared upconverter designs, both pixel-less and pixel-lated hybrid infrared imaging devices are presented, with experimental results, in this thesis. The pixel-less hybrid infrared imaging upconverter suppresses the lateral carrier diffusion by using a hybrid Schottky junction with an intrinsic interconnection layer between the inorganic and organic parts. The device was fabricated in one large-area mesa and proved that the emitting light spatially correlated with the infrared imaging shone at its back. This device is the first-ever hybrid pixel-less infrared upconverter to successfully demonstrate the imaging of infrared patterns. In contrast, the pixel-lated device consisted of 128 by 128 pixels, and each pixel was an individually working infrared upconverter that integrated a heterojunction phototransistor (HPT) and an organic light emitting diode (OLED). The HPT provides not only the photoresponse upon incoming infrared light but also an amplification of the photocurrent. The pixel-lated device also successfully demonstrated the first-ever upconversion of infrared light, up-converting a light with a wavelength of $1.5\mu m$ to $520nm$.

Acknowledgements

I would like to thank my supervisor Professor Dayan Ban for his guidance. My research would not be possible without my supervisor's support. Besides the professional training of conducting research given by Professor Dayan Ban, he also taught me important personal lessons, which will be invaluable in all of my future endeavours. I would also like to thank Professor Irene Goldthorpe and Professor Hany Aziz for their time and interest to attend my seminar and read my thesis. Suggestions from them were extremely important for me to complete this thesis. I would like to thank University of Waterloo for supporting my study and research financially. I would also like to express special appreciation to Richard Barber for his patience and instructions while I working in the Giga-2-Nano Laboratory.

I am especially indebted to the collaborators at University of Toronto for their time and efforts assisting me on my project: Professor Zhenghong Lu, Michael G. Helander, Zhibin Wang, and Jacky Qiu. Their expertise and experience on organic layers research were one of the most important parts of this collaborative research.

I must thank my former colleague Jun Chen for his constant support for my research. Many detailed explanations from him and in-depth discussions with him made me more confident on my own research. Also thanks to my current colleagues in Professor Dayan Ban's group: Ghasem Razavi, Rudra Dhar, Guocheng Liu, Chao Xu, and Hao Wang.

Finally, this thesis is dedicated to my family, my girlfriend, especially my dear parents, Jun Tao and Jia Yue for their unconditional love and encouragement during the past two years.

Table of Contents

List of Figures viii

1 Introduction 1

1.1 Background 1

1.2 Infrared photodetector 3

1.3 Infrared upconversion 5

1.4 Operation principle of infrared upconverters 7

1.4.1 Photodetector 7

1.4.2 Light emitting diode (LED) 9

1.4.3 Performance of the entire upconversion device 11

1.5 Development of Upconversion device 11

1.5.1 Proof of concept 11

1.5.2 Wafer fusion technology (direct wafer bonding) 13

1.5.3 Organic upconversion device 16

1.5.4 Hybrid inorganic-upconversion device 22

1.5.5 The implementation of embedded metal mirror 25

1.5.6 The enhanced photodetector - heterojunction photo-transistor (HPT) 27

1.6 Infrared upconversion imaging devices 32

1.7 Thesis Overview 39

2 Fabrication **40**

2.1 Wafer scribing 41

2.2 Wafer surface cleaning 42

2.3 Photolithography - mesa and window patterning 43

2.4 Wet etching - mesa etching and window opening 46

2.5 Deposition - silicon nitride, metal contact/metal mirror, and organic layers 48

3 Pixel-less Imaging Device **54**

3.1 Motivation 54

3.2 Device fabrication 58

3.3 Working principle 60

3.4 Imaging measurement system 61

3.4.1 Laser system 63

3.4.2 Alignment 64

3.4.3 Camera system 67

3.5 Pixelless Imaging Result . . . 68

3.6 Conclusion . . . 74

4 Pixel-lated Imaging Device **75**

4.1 Motivation . . . 75

4.2 Device fabrication . . . 77

4.3 Pixellated imaging results . . . 79

4.4 Imaging result analysis . . . 82

4.5 Challenges and future work . . . 87

4.6 Conclusion . . . 89

5 Summary and contributions **90**

References **92**

List of Figures

1.1 Electromagnetic spectrum 2

1.2 Bandgap profile of the proposed integrated QWIP and LED[29] 12

1.3 Schematic layer structure and band-edge profile of Liu's p-i-n/LED device[43] 14

1.4 Schematic layer structure of the wafer-fused p-i-n/LED photodiode device[8] 15

1.5 Schematic view of Yase's infrared photo-responsive OLED[21] 21

1.6 Schematic cross-section view of Kim's organic IR-to-green light upconversion device[32] 23

1.7 Schematic diagram of the cross section of Ban's inorganic-organic upconverter device. Note that the thickness of the organic and inorganic layers is not to the scale. Hole transport layers consist of NPB, CuPc, and C_{60}. CuPc stands for copper phthalocyanine. NPB is N , N'-di'naphthalene-l-yl'-N , N'-diphenyl-benzidine.[11] 24

1.8 (a) Schematic cross section of Chen's inorganic-organic up-converter device with embedded metal mirror. (b) Schematic configuration of the OLED layers of the integrated devices and the embedded mirror. The layer thickness is not to the scale. C_{60} is Carbon fullerene. CuPc stands for Copper phtalocyanine. NPB is N, N'-di(naphthalene-1-y1)- N,N'-diphenyl-benzidine, Alq:C545T is light emission layer. The embedded mirror layer consists of 20 nm Ti and 200 nm Au. The top metal contact consists of LiF (1 nm)/Al (5 nm)/Ag (20 nm).[18] 26

1.9 Band diagram of Luo's integrated HPT-LED upconverter under a bias of 3 V. Solid line: dark condition (no input 1.5 μm light); dotted line: $1mW/cm^2$ 1.5 μm light incident from the InP side. Inset is the schematic of the operation of the upconversion device.[45] 29

1.10 (a) Schematic cross section of Chen's hybrid optical upconverter device with integrated InGaAs/InP HPT and OLED. Note that the thickness of the organic and inorganic layers is not to scale. The embedded mirror layer consists of 20-nm Ti and 100 nm Au. The hole injection layer (HIL) of the OLED was a 3 nm thick layer of fullerene (C_{60}). The hole transport layers (HTLs) consisted of copper phthalocyanine (CuPc) (25 nm) and N,N'-diphenyl-N,N'-bis-(1-naphthyl)-1-1'-biphenyl-4,4'-diamine ($\alpha - NPD$) (45 nm). The 30 nm thick emission zone was tris-(8-hydroxyquinoline) aluminum (Alq_3), doped with 1 wt.% 10-(2-benzothiazoly)-1,1,7,7-tetramethyl-2,3,6,7-tetrahydro-1H,5H,11H [1]benzo-pyrano [6,7,8-ij]quinolizin-11-one (C545T). The electron transport layer (ETL) was made of an additional 15 nm thick Alq_3 layer. The top metal contact consisted of LiF (1 nm)/Al (5 nm)/Ag (15 nm). Finally a 45 nm thick Alq_3 layer was refractive-index matching layer. No anti-reflection coating was applied to the back side of the InGaAs/InP sample. (b) The insertion of a highly reflective metal layer as an embedded optical mirror could improve the absorption and emission efficiency.[19] . . 31

1.11 Band diagram and quasi-Fermi levels of Luo's imaging up-converter under -3 V bias.[46] 33

1.12 CCD imaging of letters "NRC" obtained from Luo's pixelless imaging up-conversion device. The device is $1.5 \times 1.5 mm^2$ in size. The device was biased at -3 V at room temperature.[46] 36

1.13 Band diagram and quasi-Fermi levels of Ban's imaging up-converter under -2 V bias, assuming the average of the hole and electron quasi-Fermi levels is closer to the valance band edge at the wafer-fused interface.[9] 37

1.14 CCD image of letters "RC" obtained from Ban's pixelless imaging up-conversion device ($1.0 \times 1.0mm^2$ in size). The device was biased at 1.5 V at room temperature.[9] 38

2.1 Mesas of a upconversion after etching InP and InGaAs layers after 1st photolithography. 47

2.2 Mesas of a upconversion device deposited with silicon nitride insulating layer 1st wet etching. 50

2.3 A Kurt J.Lesker OLED cluster tool with six chambers[24] 51

2.4 Designed mask for cathode deposition mounted onto the sample holder . . 53

3.1 (a)Schematic cross-section of inorganic-organic upconverter device. Layer thickness is not to scale: C_{60} is carbon fullerene. CuPc stands for copper phtalocyanine. NPB is N,N0-di(naphthalene-1-y1)-N,N'-diphenyl-benzidine, Alq is tris-(8-hydroxyquinoline) aluminium. Alq:C545T is light emission layer. (b) Schematic band diagram across the interface[20] 57

3.2 Flow chart of fabrication step for the pixelless hybrid imaging upconversion device 59

3.3 The designed characterization system for the imaging upconversion devices. 62

3.4 Characterization results of the high power laser system 63

3.5 The optical alignment configuration for the measurement system of imaging upconversion devices. Note that the mask is put at certain distance away from the laser so that the laser beam can expand and cover the entire letter pattern on the mask. The device is put very close to the mask to avoid a loss of optical power and the distortion of laser pattern due to the laser expansion. 65

3.6 The illustration of alignment between the mask and the upconversion device. Position marks are labelled to assist positioning the mask at the back of the upconverter without seeing the actual device's active area. 66

3.7 The camera system used in our measurement system of imaging upconversion devices 67

3.8 Luminance-voltage (L-V) curve of the pixelless imaging upconverter under $1.5\mu m$ infrared illumination with $6mW/cm^2$ power [inset: the emission spectrum from the OLED of the integrated upconverter peaked at 520 nm in wavelength (green light)].[15] 70

3.9 The NIR-induced device's current as a function of device's bias under different illumination conditions.[20] 71

3.10 The comparison of the used positive mask (left) and the imaging result (right). Only the letter "R" can be recognized, and the edge is very blurry without enough clarity. 71

3.11 The imaging result of the pixelless upconversion device using a negative mask. The linkage part of the letter pattern and the edge of laser beam can be easily recognized with good contrast and clarity.[20] 72

3.12 The design and the actual photo of the negative mask with letter "IR" pattern.[16] 73

4.1 Layout of a pixellated hybrid upconversion device. The area confined in the red box is left as top contact pad for probing. Underneath the conducting Al/Ag contact pad, SiN and SiO insulating layers were inserted to avoid short circuit between bottom contact and top contact. 78

4.2 Photo of the pixellated hybrid upconversion device. It was taken when the device was biased around 40V. The central area was dark indicates the pixels there were not working properly. 80

4.3 Imaging results when the high power laser was directly placed at the back of the pixellated upconverter (left), when the laser moved (middle), and when the laser was blocked (right) 80

4.4 Imaging results when the mask was removed and the laser was directly placed at the back of device again (left), when the laser was turned off. The pixels get dim as the OLED was dying quickly. 82

4.5 Pixels of the pixellated upconversion device after imaging test. The organic layers on the working pixel (yellow arrow) were burned off. The organic layers on the non-working pixel (red arrow) remained intact. 84

4.6 I-V curve of one pixel on the HPT mesa array under different levels of illumination power. The HPT mesa array and the pixellated were from the same wafer, and they were fabricated in one batch except the OLED deposition. 85

Chapter 1

Introduction

1.1 Background

Through noticing the heat radiated from light beyond the visible spectrum, Sir Frederick William Herschel discovered infrared radiation in 1800. Since then many experiments have explored the properties of infrared light. Infrared light cannot be seen by unassisted human eyes. Its wavelength lies beyond the wavelength of red light, 750 nm, and below the wavelength of 1 mm, and can be further categorized into three sub-ranges: near-infrared (NIR), mid-infrared (MIR), and far-infrared (FIR), as illustrated in FIG. 1.1. Up until now many different applications, such as infrared imaging, heating, and vibrational spectroscopy, have been developed rapidly in all ranges through utilizing the properties of infrared light, and among all of them, infrared imaging has become one of the most important applications since it opens up a new spectrum for observation[1, 46, 8, 7, 9]. Infrared imaging can be used in many fields: in the military it is used for night vision able to identify living objects in dark environments; in scientific research it helps astronomers

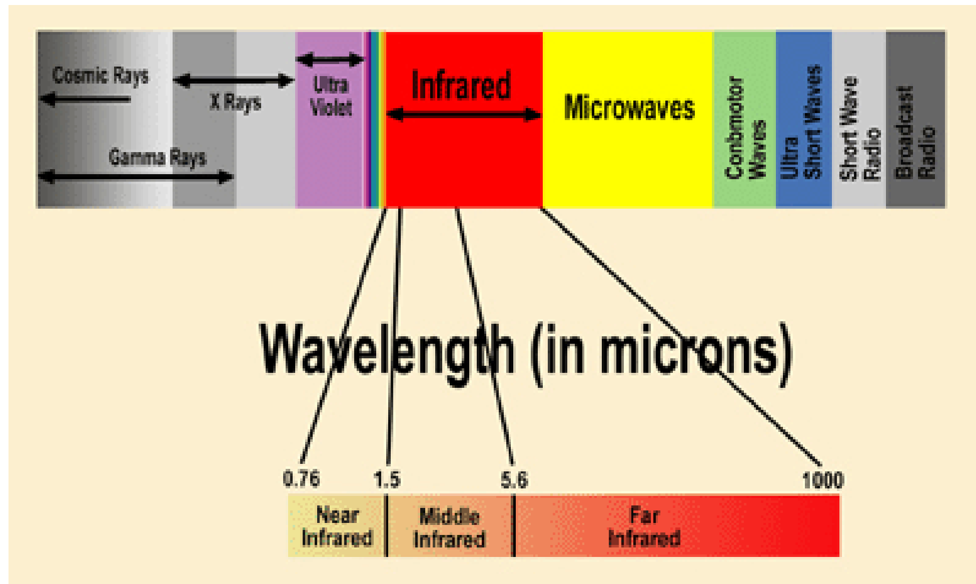

Figure 1.1: Electromagnetic spectrum

observe celestial objects through their infrared spectrum for the study of deep space; in industry it helps maintenance technicians locate overheating and overstressed parts so as to eliminate potential hazards; in daily life, it can be applied to night surveillance systems for home security, and elsewhere. Infrared imaging is widely used in these applications mainly because of several physical properties of infrared light: firstly, infrared imaging has great coverage. For all objects under 1000 K, the blackbody-emitted radiation peaks at the infrared wavelength range, which enables the detection of many objects in different settings; secondly, thanks to the long wavelength, infrared light can pass through obstacles for distant detection through air because there is a transparent window of the earth atmosphere where the infrared light is not significantly absorbed by its carbon dioxide and water; lastly, the absorption spectra of chemicals are unique for different chemical structures.

However, although infrared imaging has great demands in numerous fields, it cannot be achieved with regular commercial imaging devices, such as a charge coupled device (CCD)

or a complementary metal-oxide-semiconductor (CMOS) real-time imaging device, which theoretically, can only detect light with a wavelength up to 1 μm. Furthermore, an infrared filter is normally installed in front of most of those devices to block the incoming light of the infrared range in order to protect the user's eyes. Therefore, new technologies are developed specifically for infrared imaging, and the current standardized infrared imaging device involves a set of lens for light collection, a focal plane array (FPA) for infrared light detection, a read-out-integrated circuit (ROIC), a central processing unit (CPU), and a display to show the detected infrared images. The focal plane array is an array of infrared detectors, which convert infrared light to electrical signals to be spatially correlated by the ROIC at each pixel, while the CPU is responsible for translating the read-in signal array to an image and delivering it to the display.

1.2 Infrared photodetector

As mentioned in the previous section, infrared photodetectors consisting of a focal plane array at each pixel play a central role for infrared imaging, converting infrared light to electrical signals to be displayed. It is necessary to understand an infrared photodetector's operating principle, by which detectors can be categorized into two different types: the thermal detector and the photonic detector. The thermal detectors take advantage of the temperature dependent phenomenon caused by the incident IR radiation, and the thermal effects may involve changes in resistance, thermoelectric effect, thermal expansion, etc. Although the thermal detectors are widely used because of their simple implementation, their response times and sensitivities often make them inferior to photonic detectors. The photonic detectors are made of semiconductors with narrow band gaps that fit the photonic energy of light at certain infrared ranges, where the electronic excitations usually take

place due to the absorption of infrared photons. There are mainly two different photonic detector types: the photoconductive photodetector and the photovoltaic photodetector[60]. An infrared photoconductive photodetector uses a material that becomes more conductive due to the increase of the free excited electrons when it absorbs optical power of light in the infrared range. In an infrared photovoltaic photodetector, the infrared photon absorption excites the electron-hole pairs, which are separated by the built-in electric field at the depletion region, resulting in a change of voltage.

The detection range of a photodetector is mainly determined by the material of a detector's absorption layer. PbS is the 1st semiconductor material that demonstrated a photo-detection of infrared light ($3\mu m$). Gradually, silicon became dominant for making photodetectors for visible and near infrared light of a wavelength below $1\mu m$ due to the mature technology for its industrial fabrication and manufacturing. Normally, Si, Ge, $GaAs$, $InSb$, $InGaAs$ and $HgCdTe$ are all popular semiconductors used for high performance detectors, which provides a variety choice of infrared detection range[53, 56, 4]. A technique of inherent bandgap engineering expands the detection range of semiconductor photodetector for infrared detection. One example is that one can detect light of a wavelength from $700\mu m$ to $3\mu m$ with a InGaAs photodetector by changing the semiconductor composition's rich ratio: $In_{0.53}Ga_{0.47}As$ for the 1.55 μm photo-detection. Different structures have been developed for infrared photodetectors. P-i-n photodiodes, metal-semiconductor-metal detectors, and bipolar phototransistors are the most popular ones, having the advantages of wide-ranges of detection, easy fabrication steps, and high performance. However, a smaller bandgap of materials required for infrared photo-detection of longer wavelength will cause larger lattice constants and weaker atomic bonds, which will make the semiconductors become extremely brittle, and that will also increase the difficulty for fabrication with the traditional epitaxial growing process. Therefore, photodetectors

using extrinsic semiconductors are developed to extend infrared detection. Because the ionization energies for donors/acceptors are typically much lower than the energy gap between the conduction band and the valence band, they can be used to detect photons with a very long wavelength (small energy). Another method to detect light with longer wavelengths is to take advantage of intra-band photo-electron interactions. One example is the quantum-well photodetector, which has confined heterostructures that lead to distinct energy levels for electrons in quantum wells. Those energy levels also have much smaller gaps compared with the gap between a intrinsic semiconductor's conduction band and valence band. Therefore, the intra-band transitions of electrons can also be used for long-wavelength photo-detection[40].

1.3 Infrared upconversion

Light in the infrared range is of great interest due to many potential applications, and a normal silicon-based camera cannot achieve the infrared detection for light of over 1 μm wavelength due to silicon's wide bandgap. Currently, the industrial standard infrared imaging system is to detect infrared scene by using the focal plane array that consists of an array of infrared photodetectors and a silicon read-out-integrated circuit, which are bonded by use of indium bumping technology, and the output the detected signals optically through LCD or other imaging devices. There are several disadvantages that limit the development of the current infrared imaging devices. Firstly, the fabrication is complicated, and it is a one-piece-a-time process to connect the focal plane array with a ROIC pixel by pixel through indium bumping, which increases the cost of one device significantly; secondly, the device is difficult to scale down while maintaining the same number of pixels. Because the density of indium bumping is proportional to the number of pixels of an FPA, options

are limited to increasing the number of pixels for a better resolution while increasing the size of device, or to scaling down the device but sacrificing the resolution by shrinking the number of pixels; furthermore, the indium bumping causes more noise and also consumes more power at each pixel. Although the extra power at each pixel is often acceptable, the power expenditure across a large array is often less tolerable. Moreover, the current infrared imaging system is extremely expensive compared with a normal camera. For example, an infrared imaging system with a resolution of 1M pixels (1024 by 1024) normally costs for over 200 thousand dollars, yet a normal camera with over 10M pixels costs for only several thousand dollars.

An infrared upconversion device was then proposed as an alternative to the current imaging device[64, 63, 38]. In the beginning, an infrared upconverter was two p-i-n junctions connected back to back. When applying bias, the reverse-biased p-i-n junction functions as a photodetector where the incoming infrared photons are absorbed at its intrinsic layer. The absorbed photons excite carriers, which flow into the forward-biased p-i-n junction that functions as an LED. The intrinsic layer of the forward-biased p-i-n junction works as an active layer of an LED, which releases the carrier energy back as photons with a wavelength in the visible range. A traditional camera with a silicon-based CCD or CMOS can then capture the emitted light from the upconversion device. Since the concept of upconversion was proposed, the infrared upconverter has attracted much interest, mainly due to its simple processing, the much lower cost, and its potential to perform with a much higher resolution. Because the up-converted image becomes visible the infrared imaging only requires a normal camera, which has been developed with a resolution of multi-mega pixels. Therefore, with an infrared upconverter in front of a commercial camera, one can theoretically capture an infrared image with a multi-mega-pixel resolution. In real practice, there are several factors that describe the performance of an upconverter. Since the

concept was proposed, many techniques and different structures have been tried to realize infrared upconversion[57, 12]. The next several sections will introduce the underlying physics of an upconverter, and will introduce those performance-deciding factors in detail.

1.4 Operation principle of infrared upconverters

1.4.1 Photodetector

The optical-electrical process takes place within a photodetector. The photodetector absorbs the incoming photons, which excite electron-hole pairs, hence generating photocurrent on the other side. The photodetector typically consists of three layers, one intrinsic layer sandwiched by one n-doped layer and one p-doped layer. The intrinsic layer is also called absorption/active layer because most of the optical absorption processes happen in this layer, and the bandgap of the intrinsic layer hence determines the absorption wavelength. The thickness of the intrinsic layer is designed to be much larger than that of the n-doped and p-doped layers so as to maximize the absorption of incoming photons. In addition, compared with the intrinsic layer, the n-doped and p-doped layers are made of a different material with a larger bandgap so that they will not absorb the incoming photons of desired input wavelength. However, the bandgap difference between layers cannot be too large, since the excited electrons must not be confined by the energetic barrier due to the bandgap difference, and can be successfully injected to the light emitting diode.

The photon conversion efficiency, usually defined as the ratio of the number of excited electrons and the incoming number of photons, is used to describe the performance of a photodetector; with measured power of incoming light and outgoing current the efficiency

can be calculated by

$$\eta_{conv} = \frac{I_{photo}/q}{P_{in}/h\nu}, \tag{1.1}$$

where I_{photo} is the photocurrent (A), η_{conv} the photon conversion efficiency, P_{in} the input light power (W), h the Planck constant, ν the frequency of input light, and q the charge of electron. On the other hand, the photon absorption efficiency of a p-i-n photodetector, can be calculated by

$$\eta_{abs} = (1 - R)(1 - e^{-\alpha d}), \tag{1.2}$$

where R is the reflectance at the air/photodetector interface, α is the material absorption coefficient decided by doping profile and light frequency, and d is the absorption layer thickness. $(1 - R)$ gives the fraction of photons entering the photodetector (that is, not reflected), and $(1 - e^{-\alpha d})$ gives the fraction of transmitted photons being absorbed. Since it is normally assumed the number of absorbed photons is equal to the number of excited electrons, the multiplication of the two terms yields the photon conversion efficiency. Combining Eq. 1.1 and Eq. 1.2, the output photocurrent can then be calculated by

$$\begin{aligned} I_{photo} &= \eta_{conv}\eta_{abs}(\tfrac{P}{h\nu})q \\ &= \eta_{conv}(1 - R)(1 - e^{-\alpha d})(\tfrac{P}{h\nu})q, \end{aligned} \tag{1.3}$$

Moreover, the performance of photodetector is often characterized by its responsivity, $\Re$, defined as the ratio of output current vs. the incoming light power, in units A/W. From Eq. 1.3, we have

$$\begin{aligned} \Re &= \tfrac{I_{photo}}{P} \\ &= \eta_{conv}(1 - R)(1 - e^{-\alpha d})\tfrac{q}{h\nu} \\ &= \eta_{conv}(1 - R)(1 - e^{-\alpha d})\tfrac{q\lambda_{in}}{hc}, \end{aligned} \tag{1.4}$$

where λ_{in} is the wavelength of incoming light.

1.4.2 Light emitting diode (LED)

In addition to the optical-electrical processes, the electrical-optical processes in the LED part are equally important for the upconverter. For either an inorganic LED or an organic light emitting diode (OLED), the structure is basically a three-layer p-i-n heterojunction. The middle intrinsic layer has a narrower bandgap, compared to the p-doped and n-doped layers, As a result, injected electrons and holes are confined in the middle intrinsic layer and are expected to recombine to emit photons at the desired wavelength. Since most of the electrical-optical processes takes place in the middle intrinsic layer it is also called the active layer for the LED.

The performance of a LED is mainly determined by the following processes: the current injection into the active layer of the LED, the generation of photons, and photon escaping from the device. Engineers have defined the following parameters to address the above processes: current injection efficiency, η_{inj}, representing the percentage of electrons effectively injected into the LED; internal quantum efficiency, η_{int}, the percentage of injected electrons that lead to photon emission; and light-escape probability, η_c, the percentage of photons finally escaping out of the device to be seen. The common quantity to measure LED overall performance is the external quantum efficiency, which is defined as the ratio of output light power vs. the input photocurrent, with units W/A:

$$\begin{aligned} \eta_{ext} &= \frac{P_{out}}{I_{photo}} = \frac{\#photons}{\#electrons} \cdot \frac{h\nu}{q} \\ &= \eta_{inj}\eta_{int}\eta_c \frac{h\nu}{q}, \end{aligned} \tag{1.5}$$

where P_{out} is the optical output power, and I_{photo} is the injection current. Here the product of η_{inj}, η_{int}, and η_c gives the ratio of output photons over injected electrons.

The light-escape probability is closely related to the material used for the air/LED

interface, which can be approximated by

$$\begin{aligned}\eta_c &= \tfrac{1}{4}(sin\theta_c)^2(1-(\tfrac{n_s-1}{n_s+1})^2) \\ &= \tfrac{1}{4}(\tfrac{1}{n_s})^2(1-(\tfrac{n_s-1}{n_s+1})^2),\end{aligned} \tag{1.6}$$

where θ_c is the critical angle at the semiconductor-air interface, beyond which complete internal reflection is observed, and n_s is the refractive index of semiconductor.

The internal quantum efficiency is governed by several different recombination processes occurring in the active layer: Shockley-Hall-Reed (SHR) non-radiative recombination, Auger non-radiative recombination, and bimolecular or spontaneous radiative recombination. Since bimolecular recombination is the only process that produces light, the internal quantum efficiency is given by

$$\eta_{int} = \frac{R_b}{R_{SHR} + R_b + R_{Auger}}, \tag{1.7}$$

where R_{SHR}, R_b, and R_{Auger} are the SHR, bimolecular, and Auger recombination rates, respectively, and they can be determined by the following equations,

$$R_{SHR} = A\frac{np - n_i^2}{p_0 + n_0 + 2\Delta n + 2n_i}, \tag{1.8}$$

$$R_b = B(np - n_i^2), \tag{1.9}$$

$$R_{Auger} = C(np - n_i^2)(p_0 + n_0 + 2\Delta n), \tag{1.10}$$

where A, B, and C are the recombination coefficients for the corresponding processes, n is the total electron density, n_0 is the electron density at equilibrium, and Δn is the excess electron density. Similarly, p is the total hole density, and it is the sum of the hole density at equilibrium, p_0, and the excess hole density, Δp[58, 28].

The current injection efficiency is the ratio of the effective current injected into the active region to total current, given by

$$\eta_{inj} = \frac{I_{SHR} + I_b + I_{Auger}}{I_{SHR} + I_b + I_{Auger} + I_{leak}}, \tag{1.11}$$

where I_{SHR}, I_b, and I_{Auger} are the currents for the corresponding recombination processes, and I_{leak} is the leakage current due to recombination taking place outside of the active region of the light emitting diode.

1.4.3 Performance of the entire upconversion device

The overall performance of linear photon upconversion device can be easily calculated by multiplying the responsivity of the photodetector part and the external quantum efficiency of the light emitting diode part:

$$\begin{aligned} \eta_{uc} &= \Re \cdot \eta_{ext} \\ &= (\eta_{conv}(1-R)(1-e^{\alpha d})\tfrac{q\lambda_{in}}{hc}) \cdot (\eta_{inj}\eta_{int}\eta_c \tfrac{h\nu_{out}}{q}) \\ &= (1-R)(1-e^{\alpha d})\tfrac{\lambda_{in}}{\lambda_{out}}\eta_{conv}\eta_{inj}\eta_{int}\eta_c, \end{aligned} \tag{1.12}$$

which gives the overall upconversion power efficiency, η_{uc}, in a unit of W/W.

1.5 Development of Upconversion device

1.5.1 Proof of concept

Liu et al. first proposed the concept of an infrared upconversion device in 1995. Instead of meeting the stringent fabrication requirements brought by indium bumping technology, his upconversion device used a quantum well infrared photodetector (QWIP) and a LED. To

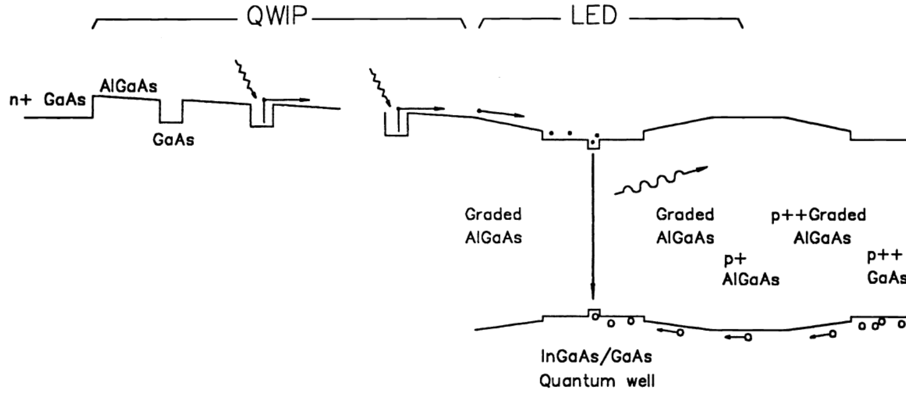

Figure 1.2: Bandgap profile of the proposed integrated QWIP and LED[29]

connect the two parts, lattice constant matching is required for the constituent materials. Unlike a p-i-n, a QWIP takes advantage of intra-band absorption that results in carriers jumping from a lower conduction intersub-band to a higher intersubband, enabling low energy absorption and allowing controlled photo-electric interactions for photons of a longer wavelength so that the device is able to detect MIR, or even FIR. As illustrated in FIG. 1.2, the QWIP was integrated with the LED in series. Liu et al. used $GaAs/Al_{0.25}Ga_{0.75}As$ for their QWIP and InGaAs/GaAs for their LED. The experimental results successfully demonstrated an MIR upconversion from light of a wavelength of 9.2 μm to 927 nm at 80 K. With further optimization, Liu's device was able to detect an optical power as low as 1.5 μW, but the overall performance was still not satisfactory as the external upconversion efficiency was only 0.8%. This was due to the low extraction efficiency of the LED incurred by the large refractive-index mismatch at the air/LED interface[29].

Later, Liu et al. proposed another upconverter design that was able to up-convert light from a wavelength of 1.5 μm to 1 μm. It was a device integrating a p-i-n heterojunction photodetector and an LED. FIG. 1.3 shows the schematic structure of this device:

the photodetector and LED were connected back-to-back, the photodetector was made of $InGaAs/InP$, and the LED was made of InAsP/InP. All layers are directly epitaxially grown onto an InP substrate, with the common layer InP in the middle. When functioning at room temperature the responsivity of the p-i-n photodetector was 2 A/W, indicating an almost 100% absorption and conversion (to photocurrent). The LED still suffered from a low internal quantum efficiency below 1%, due to the total internal reflection and the poor carrier confinement at the LED active layer, which was caused by the small bandgap difference between the cladding layers and the active layer. The poor confinement was proved by demonstrating the fact that when operating at 77 K, the internal quantum efficiency of LED was shown to be 300 times greater than the efficiency of the same device operated at the room temperature, and this discrepancy can be explained by the escape of not-well-confined carriers from the active layer to the cladding layers due to thermal energy[43].

Although both QWIP/LED and p-i-n/LED upconverters proved the concept of infrared upconversion, they were not able to provide satisfactory efficiencies. To improve the total upconversion efficiency it is critical to solve the poor carrier confinement problem of the LED, and this could be done by increasing the energy barrier height between the cladding layers and the active layer of the LED. However, this method may result in a longer wavelength emission, and also increase the strain between the layers, which should avoid exceeding the upper limit required by the epitaxial growth process.

1.5.2 Wafer fusion technology (direct wafer bonding)

Due to the lattice constant matching constraint inherent to traditional direct epitaxial growth, researchers of infrared upconversion devices found an alternative for semiconductor

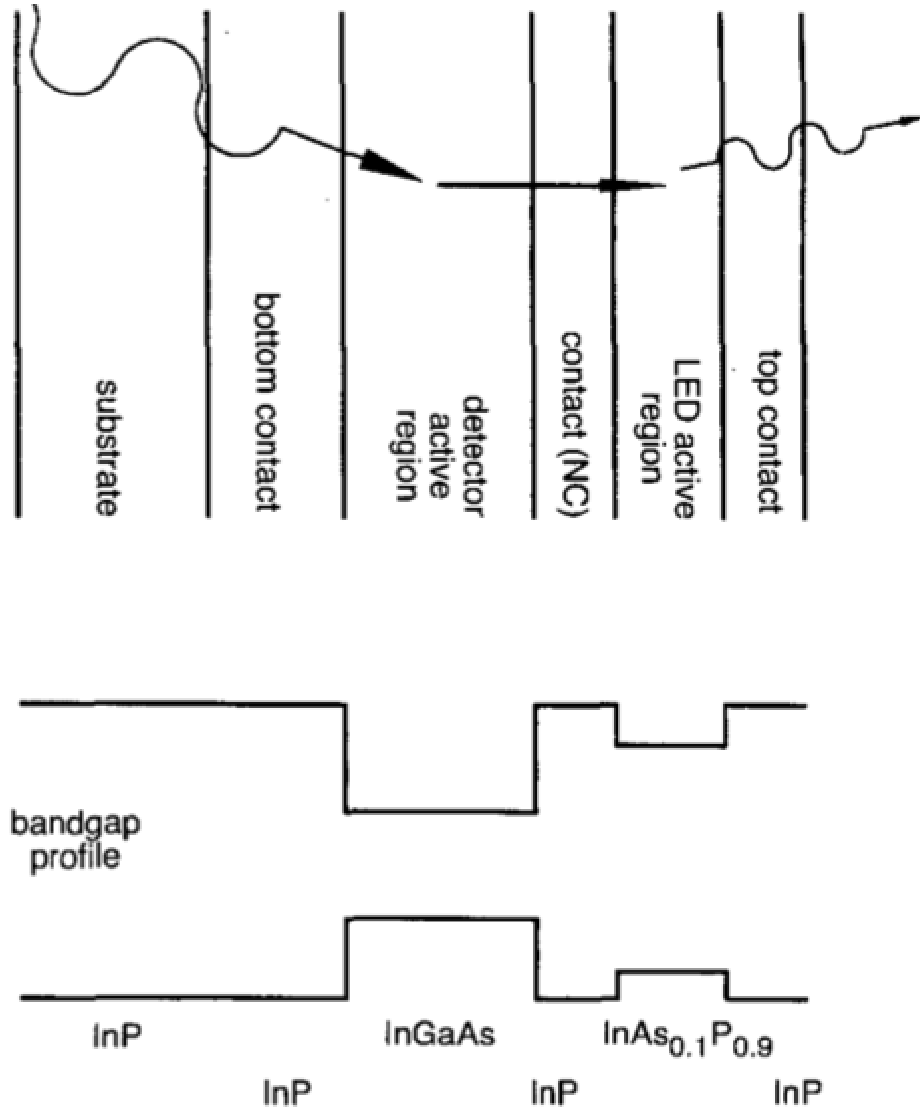

Figure 1.3: Schematic layer structure and band-edge profile of Liu's p-i-n/LED device[43]

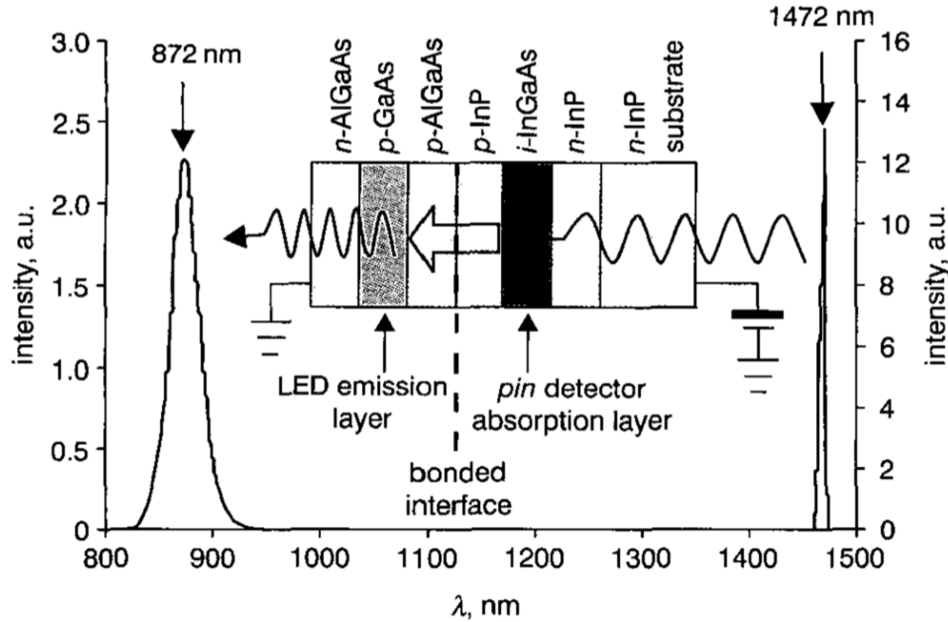

Figure 1.4: Schematic layer structure of the wafer-fused p-i-n/LED photodiode device[8]

device integration: wafer fusion. This is a wafer bonding technique used to integrate two wafers made of different semiconductors that have mismatching lattice constants, and it allows for more freely choosing the interfacial layers of the two parts. Before wafer fusion, the designed structures are grown/etched individually onto two different substrates. During the wafer fusion process, the two mating wafers need to be cleaned chemically in order to eliminate dangling bonds at the surfaces, and then they need to be dried and placed together face-to-face to initiate Van der Waals bonding. After that, the two wafers will be annealed at a high temperature for a certain amount of time in flowing N_2 under pressure; the resulting bond should be permanent. The final step of wafer fusion is to chemically etch off one of the substrates from the bonded pair[41, 8, 47, 9].

In 2003, Ban et al. integrated the p-i-n photodetector with a LED through wafer fusion, bypassing the lattice matching problem for different interfacial semiconductor layers.

Illustrated as in FIG. 1.4, an $InGaAs/InP$ photodetector and a $GaAs/AlGaAs$ LED were wafer-fused together: the direct wafer bonding of the two parts enabled Ban to choose more efficient materials for both the photodetector and LED. The results showed that the responsivity of the p-i-n photodetector was 0.8 A/W at a bias of 4 V, which was similar to an isolated photodetector of same structure, indicating that the performance of the photodetector was not compromised by the wafer fusion process. Since the newly introduced wafer integration process for upconversion devices has proved to be functional, it has potential to be applied in future upconversion devices with a higher efficiency. After experiments, the LED had an external efficiency measured to be $0.0064W/A$. As a result, the overall upconversion efficiency of this device was characterized to be 4.7×10^{-3} W/W, which agrees with the product of the responsivity of the device's photodetector and the external efficiency of the device's LED. Ban later optimized the layer doping profile of the LED according to his modelling revealing the relationship between external quantum efficiency with the layer doping concentration. After the optimization, his p-i-n/LED upconverter achieved an overall upconversion efficiency of $0.0117W/W$ at $5V$ with the enhanced LED, which had doubled the external quantum efficiency to $0.0176W/A$ compared to the previous device.[8]

1.5.3 Organic upconversion device

A brief introduction to organic semiconductors

Not only inorganic semiconductors were studied in the quest to make infrared upconversion devices, the organic semiconductors also drew a lot of attention with their rapid development and its low cost of processing. Before introducing the applications of organic semiconductors and the organic upconversion devices, it is essential to introduce the physics describing how to make an organic infrared upconversion device.

Organic semiconductors have a fundamentally different working mechanism than inorganic semiconductors. An inorganic semiconductor normally has very strong covalent bonds that extends in three-dimensional space holding the atoms together. This feature forms the conduction band and the valance band, which together give rise to the semiconducting properties. Unlike an inorganic semiconductor, the organic ones have weak intermolecular Van der Waals interactions holding the molecules together, although they do have covalent bonds within their molecules. The bonding molecules form the molecular orbitals (MOs) attributed to the linear sum from the atomic orbitals (AOs)[26]. The number of molecular orbitals are determined by the total number of AOs of each individual atoms. However, for simplicity, the linear combination of atomic orbitals (LCAO) model neglects the AOs that are localized around their nuclei for their negligible contributions to MOs, and only considers the electrons of AOs at their valance shell in modelling the MOs. The carbon-carbon MOs are extremely important to organic semiconductors, and are mostly classified either as $C-C$, the σ bonds, or as $C=C$, the π bonds. For example, in ethylene, the σ bonds are resulted from the overlap of two co-plane sp^2 AOs, while the π bonds result from the overlap of $2p$ AOs. For each kind of bonding carbon-carbon MO, there is also one kind of corresponding anti-bonding MO, π^* bond for the π bond, and σ^* bond for the σ bond. Among all the π bonding and π^* anti-bonding MOs, the bonding MO with the highest energy is called the highest occupied molecular orbital (HOMO), and the anti-bonding MO with the lowest energy is called the lowest un-occupied molecular orbital (LUMO). The conjugation of organic molecules allows the delocalization of π bonds, such as the resonance of π bonds in benzene, which derives the electronic/optoelectronic properties of organic semiconductors. An increase of conjugations will result in a smaller bandgap between HOMO and LUMO. The transport of injected carriers from one molecule to another describes the conductivity of an organic material, and the transport process is

referred to as hopping, a quantum mechanical tunnelling that depends upon the bandgap of the organic material's HOMO and LUMO.

Organic light-emitting diode (OLED)

The OLED is one of the most popular applications for organic semiconductors, and it is also one of the crucial parts of an organic infrared upconversion device. An OLED is a light-emitting diode in which the emissive electroluminescent layer is made of a film of organic compound that emits light. The concept of the OLED was proposed by Pope in 1963, when he discovered the organic electroluminescence phenomenon by applying a bias of several hundreds onto Anthracene crystal[54]. In 1987, the first ever practical OLED device was made by C.W.Tang, and that was an organic device made of a metal cathode, a transparent ITO anode, and two small organic molecule layers in between them[61]. Since then, OLEDs have attracted much attention and become more and more popular because they can achieve a very high brightness with a fairly low driving voltage, and it also has all the advantages of organic devices: flexibility, ease of processing, and low cost. To date, OLED has been put into many applications, for example, the large-area thin-film OLED display[3, 2]. In addition to the electrodes, the general structure of an OLED is very simple and mainly incorporates only a bilayer structure, consisting of one conductive layer and one emissive layer. However, to improve the performances, more layers such as hole/electron transport layers (HTL/ETL) are introduced into the OLED[59]. Because there are no intrinsic charge carriers in the organic semiconductors and all electrons and holes must be provided externally, HTLs/ETLs become extremely important for their capability to lower the energy barriers from layer to layer and achieve an efficient electron/hole injection from the electrodes into the HOMO and LUMO of the emissive layer, respectively. When an OLED is in working condition, the injected carriers at HOMO and LUMO are brought

together by the electrostatic force and recombines into a bounded state, excitons, whose decay results in a spontaneous emission of light with a frequency depending on the bandgap between the HOMO and the LUMO[49, 27].

There are two types of excitons, differentiated by their spin angular momentums. When the spin angular momentum of an exciton is zero, the exciton is in singlet state, while when the momentum is not zero, the exciton is in triplet state. Since electrons and holes are fermions with a half integer spin, statistically there are three triplet-state excitons formed for each singlet-state exciton. Normally, the decay in triplet-state is forbidden by the selection rules in quantum mechanics. Therefore, the fluorescent OLED was developed, which only takes advantage of the decay of singlet-state exciton as the source of its light emission. However, the internal quantum efficiency is capped at 25%. Later, people figured out that material that contains heavy atoms can enable the triplet-singlet transition because the atomic nuclei of the material has a strong enough magnetic field to invert the spin of the electron during spin-orbital interaction. Based on that discovery, the phosphorescent OLED was developed, which uses both triplet and singlet excitons, allowing an internal quantum efficiency of 100%.

Development of organic infrared upconversion devices

With the development of organic semiconductors, in 2001, Yase et al. reported a photoresponsive OLED combining a blue-emitting organic electroluminescent diode with a photoconductive layer of titanyl phthalocyanine (TiOPc)[50]. FIG. 1.5 presents the schematic structure of the device: the photoconductive TiOPc layer and the fluorescent blue-emitting diode, which consists of a hole transport and emitting layer made of $N, N' - diphenyl - N, N' - bis(1 - naphthyl) - 1 - 1' biphenyl - 4, 4' - diamine (\alpha - NPD)$ and an electron transport and hole blocking layer made of $2, 9 - Dimetyl - 4, 7 - diphenyl - 1, 10 -$

$phenanthroline(BCP)$, were sandwiched between the anode and the cathode, made of a layer of transparent indium-tin-oxide (ITO) and a layer of magnesium and silver, respectively. The photoconductive layer of this device worked as a photo-responsive switch to trigger the combined OLED. Therefore, when irradiating the layers with near-infrared light of a wavelength corresponding to the absorption band of TiOPc, the photo-induced carriers that are generated in TiOPc are injected into the light emission layer, which lowers the threshold voltage of emission and also enhances the light emission at a certain bias. Although this device achieved the upconversion of light from 775 nm to 477 nm at a bias above 12 V, the overall upconversion efficiency was less than 0.05% due to the low quantum efficiency for photo-detection at the TiOPc layer and the poor external quantum efficiency (typically ¡ 5%) of OLED devices in general[21].

Kim et al. proposed a new organic infrared upconversion device in 2009. Instead of using a fluorescent OLED, they used a phosphorescent green-emitter out of $fac-trix(2-phenylpyridinato)iridium(III)(Irppy_3)-doped4,4-N,N-dicarbazole-biphenyl(CBP)$ for his device. To date, the $Irppy_3$ phosphorescent emitter is one of the most efficient emitters for OLED, and has a maximum external quantum efficiency close to 20%. Additionally, they introduced a tin phthalocyanine $(SnPc) : C_{60}$ bulk heterostructure NIR photodetector, which was able to improve the efficiency of charge separation significantly[32]. Experiments proved that the external quantum efficiency of a $SnPc : C_{60}$ bulk heterojunction device can exceed 20%. The maximum photon-to-photon upconversion efficiency for this organic upconversion device was reported to be 2.7% under an irradiation of near-infrared light at a wavelength of 830 nm, a value higher than the previously reported organic upconversion device[55]. Later, the same group reported another organic upconversion device using an inorganic colloidal PdSe nancrystals as NIR sensitizer. However, just as all aforementioned organic devices above, the input near infrared light and the output visible light

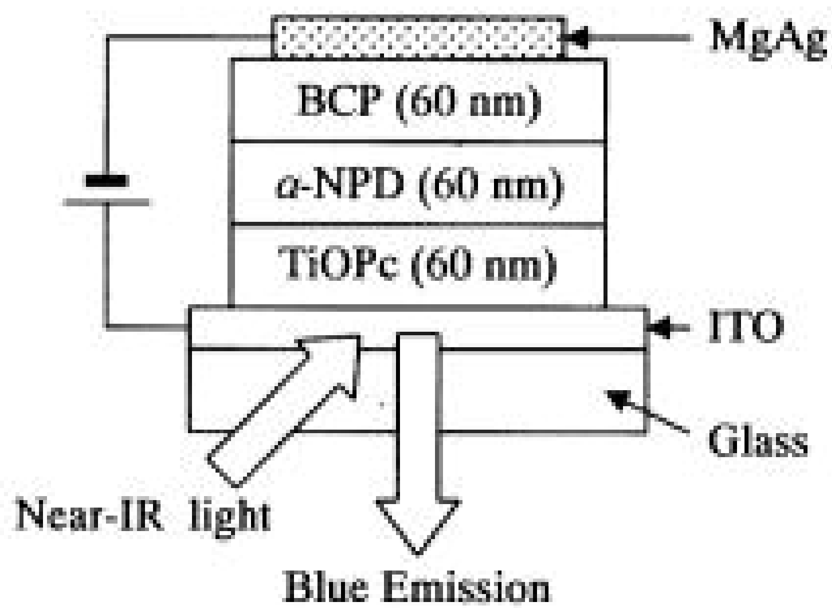

Figure 1.5: Schematic view of Yase's infrared photo-responsive OLED[21]

are limited to same side[31].

Although near-infrared upconversion has been demonstrated with several organic upconverters in recent years, several disadvantages still limit the upconversion performances for devices made of organic materials: (1) currently, neither small molecular nor polymers with low bandgaps are available for the manufacture of photodiodes working with light of a wavelength over 1 μm. Thus, the detection range and potential applications for an organic upconversion device are limited. (2) ITO is the most popular electrode used for organic devices based on bottom emission architecture due to its transparency; however, as ITO is the only transparent electrode, the infrared light must also come in at the same side as the device's light emitting, as shown in FIG. 1.6; (3) the upconversion efficiency is still too low compared with that of other inorganic infrared upconversion devices.

1.5.4 Hybrid inorganic-upconversion device

In 2007, rather than following inorganic upconverter designs, Ban et al. proposed the concept of hybrid inorganic/organic upconversion device. Organic material has topologically perfect structure that can be easily grown onto an inorganic semiconductor substrate. The easy processing of organic materials requires no lattice matching at the interfaces with the inorganic layers, and it also avoids the complicated wafer fusion process. Most importantly, it eases the limits on material choice for both inorganic and organic parts[5, 11]. With the current technology, OLEDs can cover all of the visible spectrum, and one can choose the emission wavelength by replacing the organic material of the emissive layer according to particular applications[52, 30, 65]. However, because there are no intrinsic charge carriers in the organic molecules, all charge carriers have to be injected from the cathode and the anode. As a result, efficient hole injection from the photodetector to the emissive layer of

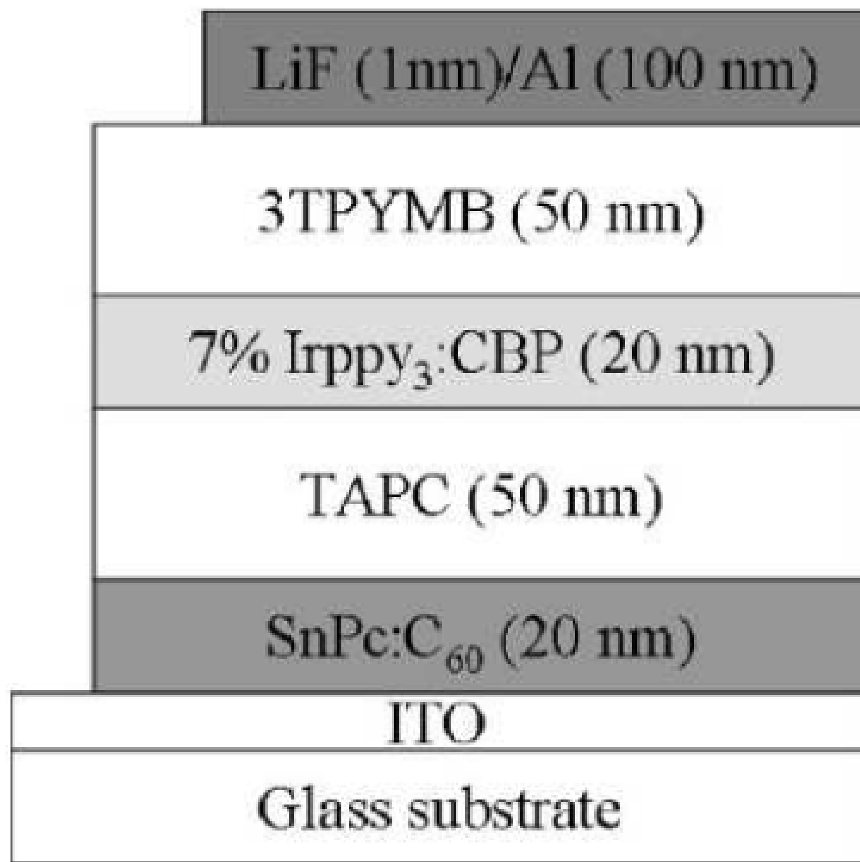

Figure 1.6: Schematic cross-section view of Kim's organic IR-to-green light upconversion device[32]

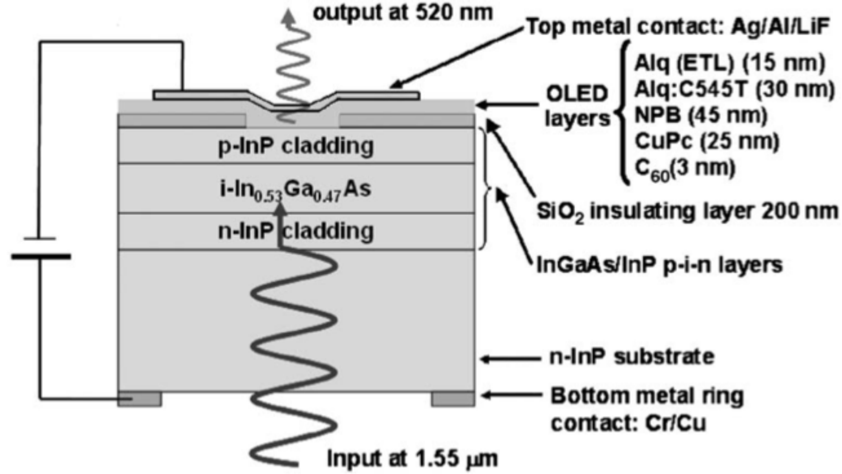

Figure 1.7: Schematic diagram of the cross section of Ban's inorganic-organic upconverter device. Note that the thickness of the organic and inorganic layers is not to the scale. Hole transport layers consist of NPB, CuPc, and C_{60}. CuPc stands for copper phthalocyanine. NPB is N , N'-di'naphthalene-l-yl'-N , N'-diphenyl-benzidine.[11]

the OLED is very critical for hybrid devices.

FIG. 1.7 shows the schematic diagram of Ban's hybrid device, for which he integrated an inorganic InGaAs/InP p-i-n photodetector with an OLED. The OLED consisted of a light emitting layer, an electron transport layer (ETL), and a hole transport layer (HTL). The light emitting layer was made of $tris-(8-hydroxyquinoline)aluminum(Alq)$ doped by (2-benzothiazoly)-1,1,7,7-tetramethyl-2,3,6,7-tetrahydro-1H,5H,11H-[1]benzo-pyrano[6,7,8-ij]quinolizin-11-one (C545T), and the ETL was made of a layer of Alq. The HTLs were specially designed and optimized to be a three-layer structure containing a N,N'-di(naphthalene-l-yl)-N,N'-diphenyl-benzidine (NPB) layer, a copper phthalocyanine (CuPc) layer, and a fullerene (C_{60}) layer. Compared with other HTL configurations, experimental results showed that

hole injection from the photodetector to the emissive layer of the OLED was enhanced by the existence of both the $CuPc$ and the C_{60} layer. Besides optimization of the HTL layers, special surface treatments were also applied to the inorganic layer at the integration interface to secure the hole injection. A surface passivation with $(NH_4)_2S$ was used to reduce the dangling bond states at the inorganic semiconductor surface in order to reduce carrier trap density. The passivation also increased the surface Fermi level of the inorganic interfacial layer, which lowered the interfacial energy barrier height. Both outcomes from passivation enhanced hole injection from the p-type InP layer of photodetector to the emissive layer of the OLED. The experiments confirmed the improvements brought by the surface passivation and showed an increase in luminance efficiency of the OLED and a drop of the device's turn-on voltage for the device that went through the passivation step. In the end, Ban's near-infrared p-i-n/OLED upconversion device demonstrated an infrared upconversion from 1.5 μm to 520 nm, with an overall upconversion efficiency of 0.007 W/W at 20 V, which indicates a good electrical connection between the inorganic and the organic parts for the hybrid architecture[5, 11].

1.5.5 The implementation of embedded metal mirror

Based on Ban's concept of hybrid upconversion devices, Chen implemented an embedded gold (Au) mirror between the inorganic photodetector and the organic light-emitting diode in 2008. In general, metals all have high reflectance. Gold has a reflectance of almost 100% for infrared light, and a reflectance of around 40% for light with a wavelength below 500 nm. Although Au's reflectance for light at visible range is not as high as its reflectance for light at infrared range, the stability of Au outperforms any other metal's so that the deposition of Au is much safer and will not damage the underneath layers. Therefore, its

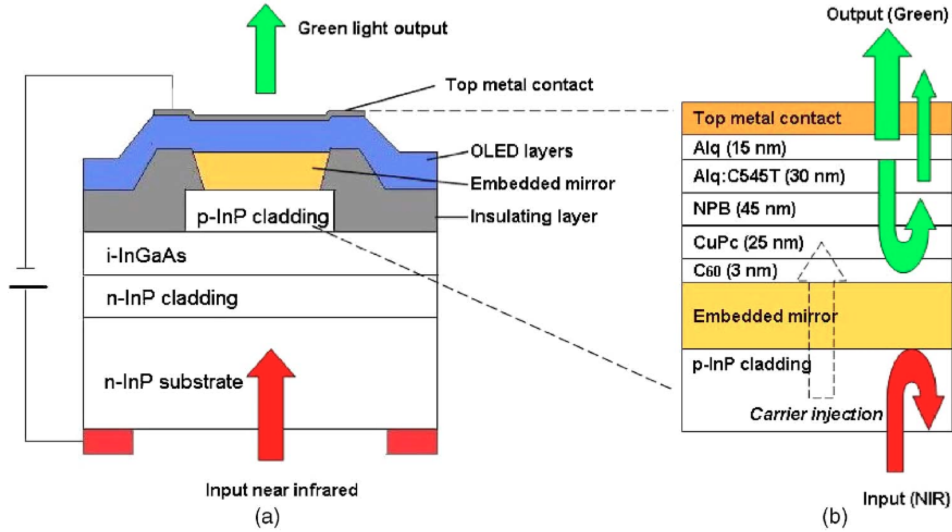

Figure 1.8: (a) Schematic cross section of Chen's inorganic-organic up-converter device with embedded metal mirror. (b) Schematic configuration of the OLED layers of the integrated devices and the embedded mirror. The layer thickness is not to the scale. C_{60} is Carbon fullerene. CuPc stands for Copper phtalocyanine. NPB is N, N'-di(naphthalene-1-y1)- N,N'-diphenyl-benzidine, Alq:C545T is light emission layer. The embedded mirror layer consists of 20 nm Ti and 200 nm Au. The top metal contact consists of LiF (1 nm)/Al (5 nm)/Ag (20 nm).[18]

high stability and relatively high reflectivity makes Au the material of choice preferred for reflecting mirrors for light at both infrared and visible ranges. In particular, the reflectivity of Ti/Au mirror proved higher than 95% for the light with a wavelength of 520 nm[13].

FIG. 1.8 shows the structure of Chen's device: the hybrid upconverter has the same structure as Ban's device but with an embedded mirror made of gold and titanium, forming a Au/C_{60} bilayer at the interface. During operation, due to the observed photon-recycling effect, the metal mirror has two benefits: the OLED light emitted downwards was bounced

back by the mirror, which resulted in an increasing number of extracted photons and an enhancement of output optical power; the infrared photons passing through the absorption layer were also bounced back by the mirror to be reabsorbed, and that increased the detection efficiency as well as the responsivity of the p-i-n photodetector[22]. Moreover, because gold and titanium have high electrical conductivities, the embedded mirror provides a good electrical connection between the inorganic photodetector and the organic LED. The total upconversion efficiency of this device was measured to be 0.015 W/W at 11.5 V, double the upconversion efficiency of Ban's device without the embedded mirror, showing that the recycling effect brought by the metal mirror substantially improved performance. During experiment, a red shift of emission light due to micro-cavity effects caused by the metal mirror and the top metal contact was also observed by Chen. This shift lead to an upconversion of light from a wavelength of 1.5 μm to 543 nm rather than to 520 nm, which was the original OLED design's output[18].

1.5.6 The enhanced photodetector - heterojunction photo-transistor (HPT)

In addition to the implementation of the embedded mirror and the optimization of the OLED, research in designing a more efficient and sensitive photodetector with a high responsivity for the upconversion devices has been conducted before the introduction of the hybrid devices. In 2006, Luo et al. chose a heterojunction photo-transistor (HPT) over the p-i-n photodiode as the photodetector for their upconversion device because the HPT is able to amplify the photocurrent, and hence improve the performance of the infrared upconverter[45].

An HPT is a bipolar junction transistor (BJT) with different materials used for its

emitter, base, and collector regions. Instead of having an incoming electrical signal at its base terminal, it takes in optical signals, leaving the base terminal electrically disconnected. The structure is two back-to-back connected p-n junctions. There are two different kinds of HPT, the n-p-n HPT and the p-n-p HPT, according to their different layer doping profiles. A n-p-n HPT has both its emitter and collector n-doped, and has a p-doped base. While a p-n-p HPT has reversed doping. Both of the two HPT types are known for their capability to amplify the incoming optical signals[44].

When the HPT operates at the forward-active mode, its base-emitter junction is under a forward bias, but its base-collector is under a reverse bias. Normally, the emitter is heavily doped, and the forward bias at the base-emitter junction allows the majority of the carriers from the emitter to be injected into the base, becoming the minority in the base. The base, however, has a lower doping concentration and is very thin so that the injected minority carriers can survive recombination with the base's majority carriers, and diffuse to the base-collector junction. Besides the extrinsic doping, the majority carriers of the base are also injected from the base-collector junction as the photo-induced carriers that are generated under illumination. This portion of majority carriers (of the base), of which the number is proportional to the optical power of illumination, also recombines with the minority injected carriers from the emitter and results in an even sharper decrease in the minority carrier concentration from the emitter to the base, which drives a more rapid minority injection by diffusion. Finally, the minority carriers that reach the base-collector junction are swept into the collector by the electric field across the depletion region and become the amplified signal.

As illustrated in FIG. 1.9, Luo integrated the InGaAs/InP HPT with a GaAs/AlGaAs LED through wafer fusion. Using this structure, an infrared upconversion for light from a wavelength of 1.5 μm to $0.87 \mu m$ was demonstrated. The HPT amplified the photo-

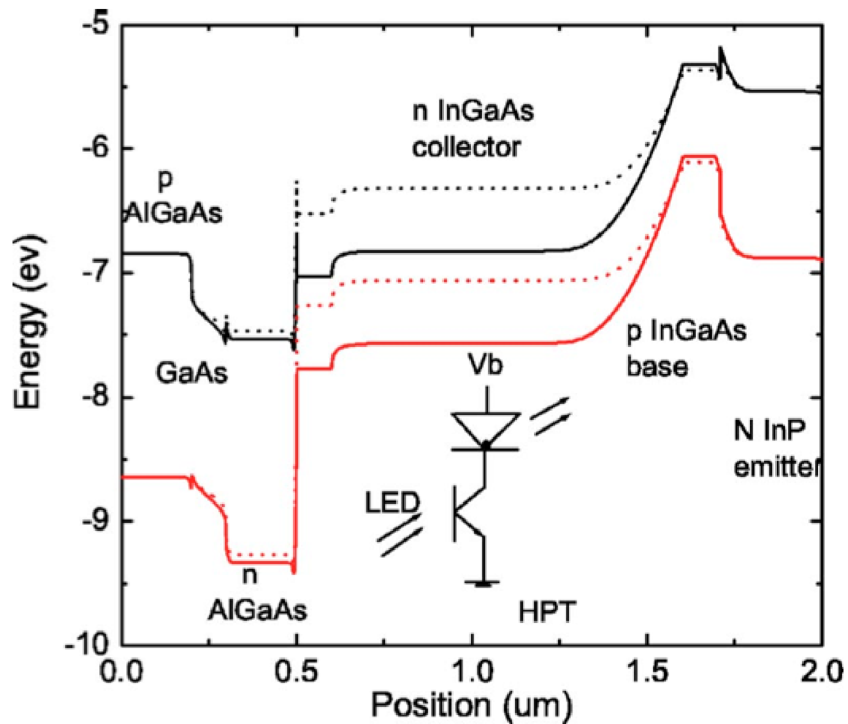

Figure 1.9: Band diagram of Luo's integrated HPT-LED upconverter under a bias of 3 V. Solid line: dark condition (no input 1.5 μm light); dotted line: $1mW/cm^2$ 1.5 μm light incident from the InP side. Inset is the schematic of the operation of the upconversion device.[45]

induced current under a low power irradiance with a gain of 20, and an overall upconversion efficiency of $0.07W/W$ was achieved at $3V$ with an optical power input of $2.2mW/cm^2$. The reduced optical gain was mainly attributed to the undesired recombination current at the depletion region of the base-collector junction[45].

The hybrid upconverter with HPT was tried later by Chen et al. Instead of using an inorganic LED, Chen deposited a green-emitting OLED on top of a p-n-p InGaAs/InP HPT. Chen's device also incorporated an embedded mirror, and the optimized structure of the HTL for the OLED. With this structure (FIG. 1.10), the HPT amplifies the photocurrent induced by the infrared irradiation, the embedded mirror recycles the incoming light and increases the number of absorbed photons, the specially designed HTL improves the transportation of photo-induced carriers from the HPT to the emissive layer of the OLED, and the emitted photons at the OLED are recycled again by the embedded mirror and extracted from upconversion device. The responsivity was measured to be $7.5A/W$ under a bias of $12V$ with an input optical power of $1mW/cm^2$, the external efficiency of OLED was $0.02W/A$, and the overall upconversion efficiency was $0.15W/W$, a ten-fold improvement compared to his previous device without an HPT, and double the performance compared with Luo's inorganic HPT/LED upconversion device[19, **?**].

Although the responsivity of photodetectors and the overall upconversion efficiency have been significantly enhanced with the implementation of HPT, the performance was still not sufficient for real practice. Therefore, Chen et al. further optimized the HPT's structure to achieve better performance for their upconversion device in 2010. The optical gain of the HPT is given by

$$g = \frac{I_C}{q}\frac{h\nu}{P_{in}} = \eta(1+\beta), \tag{1.13}$$

where I_C is collector current, q is electron charge, $h\nu$ is the energy of incident photon, P_{in} is the input optical power, η is the quantum efficiency, and β is the common emitter

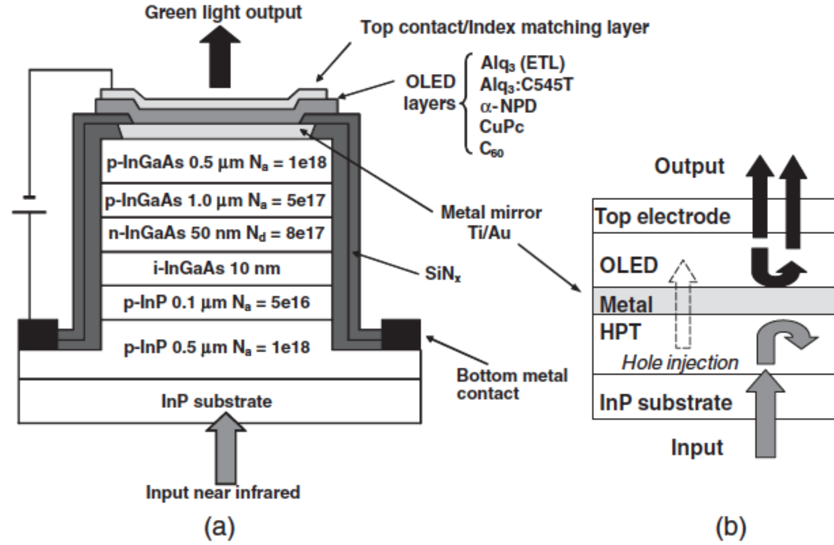

Figure 1.10: (a) Schematic cross section of Chen's hybrid optical upconverter device with integrated InGaAs/InP HPT and OLED. Note that the thickness of the organic and inorganic layers is not to scale. The embedded mirror layer consists of 20-nm Ti and 100 nm Au. The hole injection layer (HIL) of the OLED was a 3 nm thick layer of fullerene (C_{60}). The hole transport layers (HTLs) consisted of copper phthalocyanine (CuPc) (25 nm) and N,N'-diphenyl-N,N'-bis-(1-naphthyl)-1-1'-biphenyl-4,4'-diamine ($\alpha - NPD$) (45 nm). The 30 nm thick emission zone was tris-(8-hydroxyquinoline) aluminum (Alq_3), doped with 1 wt.% 10-(2-benzothiazoly)-1,1,7,7-tetramethyl-2,3,6,7-tetrahydro-1H,5H,11H [1]benzo-pyrano [6,7,8-ij]quinolizin-11-one (C545T). The electron transport layer (ETL) was made of an additional 15 nm thick Alq_3 layer. The top metal contact consisted of LiF (1 nm)/Al (5 nm)/Ag (15 nm). Finally a 45 nm thick Alq_3 layer was refractive-index matching layer. No anti-reflection coating was applied to the back side of the InGaAs/InP sample. (b) The insertion of a highly reflective metal layer as an embedded optical mirror could improve the absorption and emission efficiency.[19]

current gain, which is determined by emitter injection efficiency, η_e,

$$\beta = \frac{\eta_e}{1 - \eta_e}, \tag{1.14}$$

When η_e approaches unity, the common emitter current gain is given by

$$\beta = \frac{1}{cosh(W_B/L_B - 1)}, \tag{1.15}$$

where W_B is the base width, and L_B is the hole diffusion length in the base layer. Chen observed the fact that reducing the base layer thickness could increase the common emitter efficiency β, and in the end enhance the optical gain[48, 36]. He therefore reduced the thickness of HPT base layer according to Eq. 1.15. In addition, Chen also adopted double emitter layers with high-low doping profiles, which was proved to suppress recombination current at the interface of the emitter and the base and improve the efficiency of minority carrier injection across the base-emitter junction[39]. A near-infrared to visible light upconversion was demonstrated with Chen's device: the optical gain of this structure was 94, and the overall upconversion efficiency achieved $1.55W/W$ at $1.2mW/cm^2$ at a bias of $21V$. Therefore, by introducing the optimized HPT to the upconversion device for infrared detection, an external power efficiency over 100% was reached, which is another tenfold improvement based on Chen's previous upconversion design. So far, this p-n-p HPT/OLED upconverter has the highest efficiency among all infrared upconversion devices[19, **?**].

1.6 Infrared upconversion imaging devices

Although a lot of research has been conducted to achieve a high efficiency single-element infrared upconverter, to realize the infrared upconversion imaging requires not only a high upconversion efficiency, but also a high spatial resolution that gives a clear up-converted

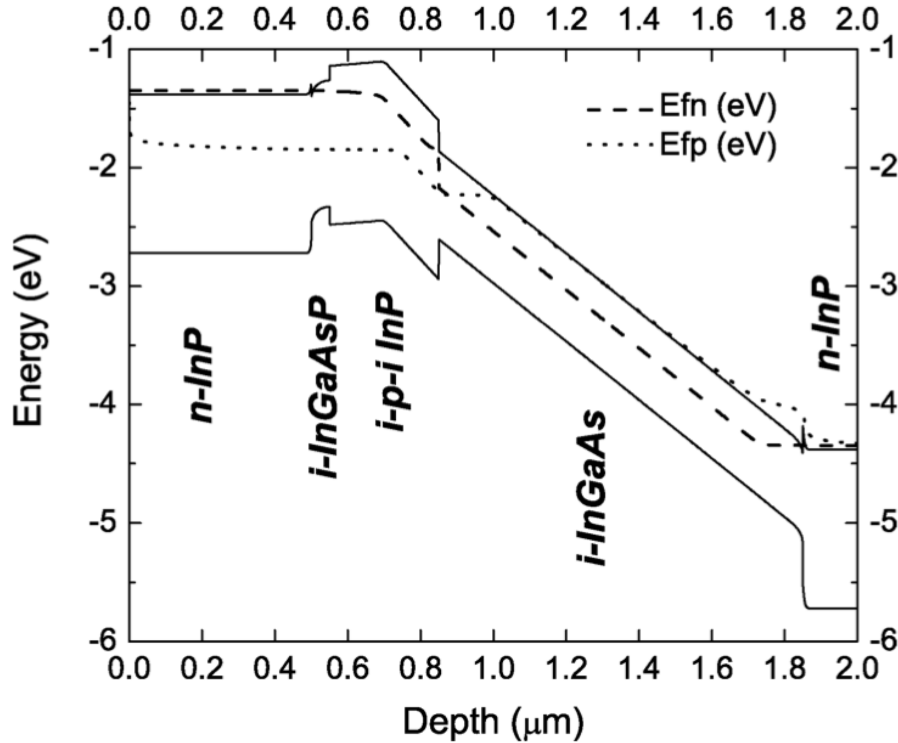

Figure 1.11: Band diagram and quasi-Fermi levels of Luo's imaging up-converter under -3 V bias.[46]

image. The spatial resolution is normally limited at the PD-LED common region, where the lateral carrier diffusion takes place. In all fore-mentioned designs, the interfacial layers of the two parts of the upconversion devices are all heavily doped in order to allow an efficient hole injection from the photodetector to the LED by providing a good electrical connection. However, a heavily doped layer normally has a good conductivity in all directions, which allows a lateral diffusion of the photo-induced carriers. A large lateral diffusion (within a plane perpendicular to the incoming infrared light/scene) will blur an image, lowering the resolution as well as the quality of the up-converted image[42].

To overcome this constraint, Luo et al. proposed an i-p-i three-layer InP configuration at the common region of the upconversion device between the photodetector and the LED part. FIG. 1.11 shows the simulation of a band diagram as well the layer structure of Luo's device. He integrated an InGaAs/InP $p-i-n$ photodiode with an $In_{0.93}Ga_{0.07}As_{0.16}, P_{0.84}$ LED through direct epitaxial growth onto an $InGaAs/InPp-i-n$ photodiode. However, unlike his previous device, of which the p-type InP layer was used as a common layer for both the p-i-n photodetector and the cladding layer of the LED, he inserted two more intrinsic InP layers that sandwiched this common layer. By doing this, the two intrinsic layers protect the photo-induced carriers from lateral diffusion, while the sandwiched p-type layer drag the diffusing carriers from the photodetector to the LED by providing enough momentum with its electric field at the depletion region. As shown in FIG. 1.11, the separation of the electron/hole quasi-Fermi levels as well as the conduction/valance band edges depict hole depletion in the common region, which predicts a significant suppression of lateral carrier diffusion at the interfaces. A good electrical connection between the photodetector and the LED by using this $i-p-i$ InP configuration at the common region was also proved with the fact that the device successfully functioned to up-convert the mid-infrared light with a wavelength of $1.5\mu m$ to the near-infrared light with a wavelength of $0.87\mu m$. The modified p-i-n photodetector has a responsivity of $0.8A/W$, and the overall upconversion efficiency of the entire device was $1 \times 10^{-4}W/W$ at a bias of $3V$. The low overall upconversion efficiency was due to the LED's low external efficiency, which was mainly attributed to the poor confinement of carriers at the active layer incurred by the small bandgap difference between the cladding layers and the light-emission layer. FIG. 1.12 shows the up-converted image with Luo's imaging upconverter. One can recognize the letter "NRC" in the up-converted letter, which indicates a fairly good resolution of the upconversion. Although this device has a low upconversion efficiency, it is the first

ever upconverter that achieved active imaging[46].

Based on Luo's device, Ban introduced the wafer fusion technology to the upconverter. The direct wafer bonding allows Ban to choose a different LED structure regardless of its interfacial material's lattice constant. Therefore, instead of using an $InGaAs/InP$ LED, Ban implemented a GaAs/AlGaAs LED. Ban also followed the i-p-i three-layer configuration for the device's common region. As shown in FIG. 1.13, here he used a layer of intrinsic InP, a layer of p-type $GaAs$, and a layer of i-type $AlGaAs$. With the modified structure the device performed well by up-converting infrared light with a wavelength of $1.5\mu m$ to a wavelength of $0.87\mu m$. The LED external efficiency was low, measured to be $5 \times 10^{-5} W/A$. However, because the single LED based on the same MBE-grown wafer also presented a very low external efficiency, it can be concluded that it is not the wafer fusion causing this poor LED performance. Fortunately, other than working as an upconverter, the entire device accidentally worked as a n-p-n phototransistor with its common region i-p-i layers working as a floating p-type base, the n-type InP as the collector, and the n-type AlGaAs as the emitter. During the experiment, the photo-induced carriers were generated at the intrinsic $InGaAs$ absorption layer, which formed a photocurrent I_{ph} flowing to the collector. In the meantime, a small amount of holes induced by incoming photons diffused into the base and recombined with electrons injected from the emitter. The recombination of the minority carriers, the electrons, and the majority hole carriers resulted in a decrease of base-emitter potentials and, therefore, more electrons were injected across the base-emitter junction under forward bias; they were later swept into the collector due to the electric field in base-collector's depletion region. With G as the dc common-emitter current gain, the total device current was therefore a sum of the photocurrent and the amplified current, $I_{ph} + GI_{ph}$. The resulted showed the internal electrical gain was over 100, and the overall upconversion efficiency of this upconverter was $0.01W/W$ at a bias of $7V$. FIG. 1.14 shows

Figure 1.12: CCD imaging of letters "NRC" obtained from Luo's pixelless imaging up-conversion device. The device is $1.5 \times 1.5mm^2$ in size. The device was biased at -3 V at room temperature.[46]

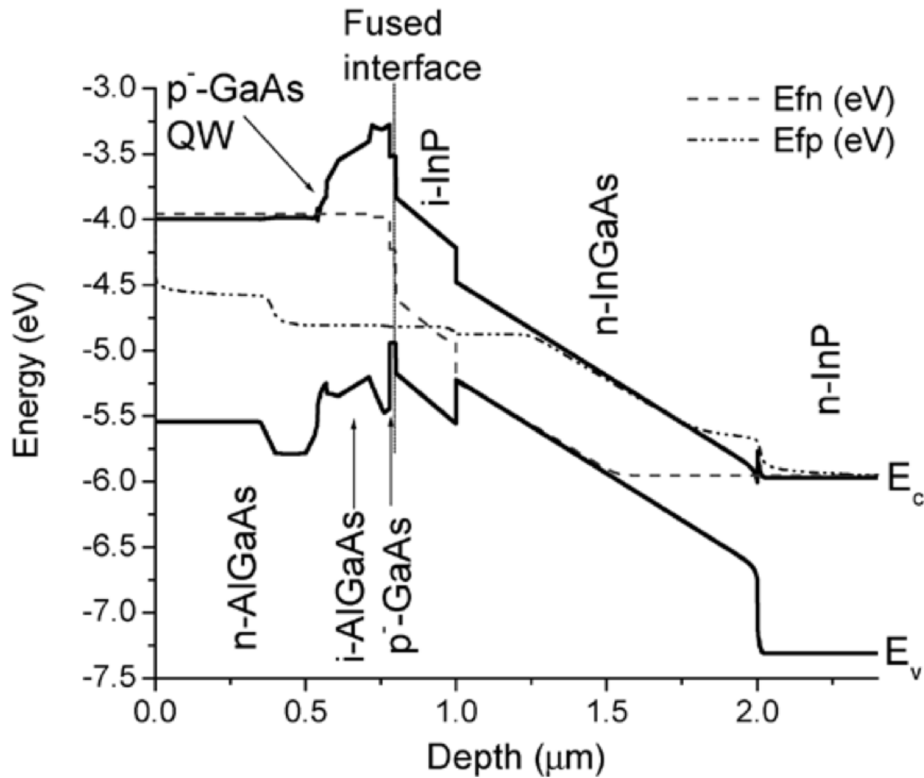

Figure 1.13: Band diagram and quasi-Fermi levels of Ban's imaging up-converter under -2 V bias, assuming the average of the hole and electron quasi-Fermi levels is closer to the valance band edge at the wafer-fused interface.[9]

the resulting image of this infrared upconversion device. With the presented good contrast and resolution, the letter "RC" can be easily recognized. Although, the efficiency is still not sufficient for applications, Ban's device has achieved the upconversion imaging without losing much of the upconversion efficiency. [9]

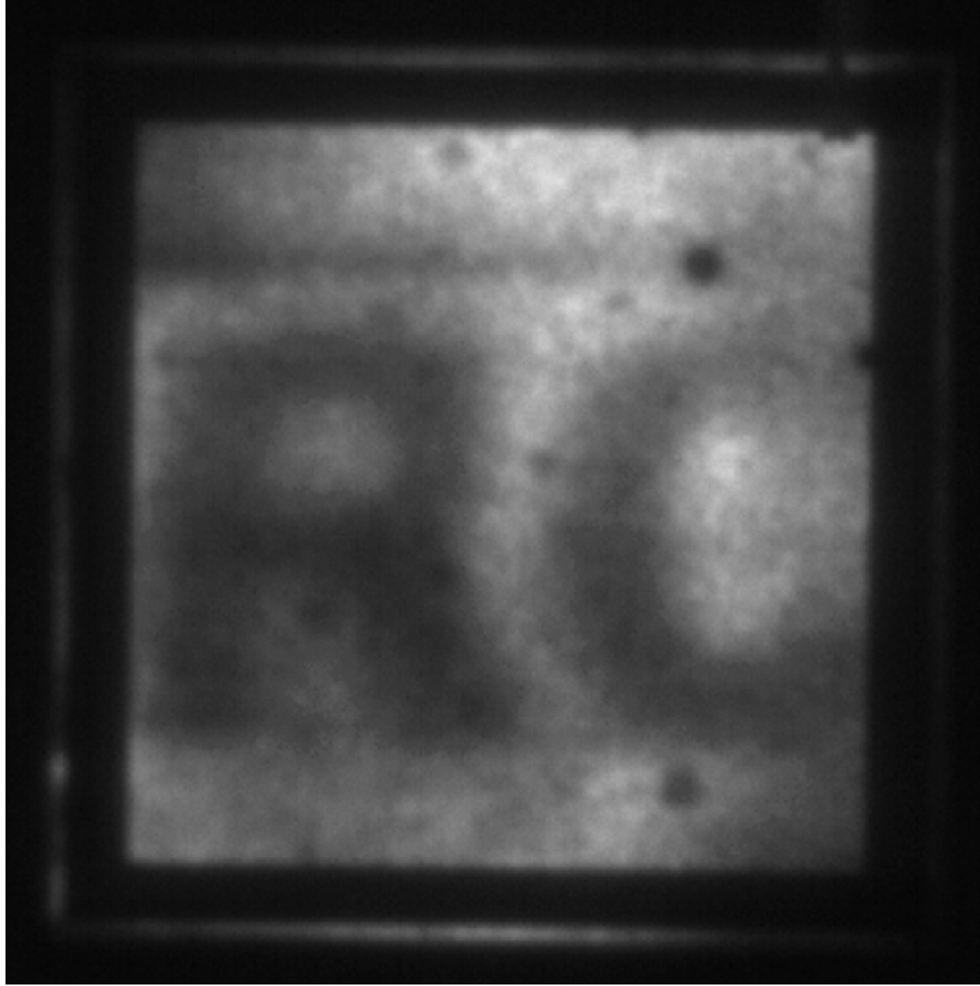

Figure 1.14: CCD image of letters "RC" obtained from Ban's pixelless imaging up-conversion device ($1.0 \times 1.0 mm^2$ in size). The device was biased at 1.5 V at room temperature.[9]

1.7 Thesis Overview

The proposed research is aimed to realize the imaging of an infrared upconversion device with high resolution while maintaining the high upconversion efficiency, and the thesis can be outlined as follows.

Chapter 1 comprehensively review the current infrared imaging technology and the development and progress of the newly proposed infrared upconversion device.

Chapter 2 lists the critical procedures for pixelless/pixellated infrared imaging upconversion device.

Chapter 3 describes the performances of the small-area Schottky-junction/OLED upconverter and then demonstrates the imaging results for the large-area Schottky-junction/OLED imaging upconversion device.

Chapter 4 describes the performances of single-element HPT/OLED upconverter and then presents the imaging results for the 128×128 pixellated HPT/OLED imaging upconversion device.

Chapter 5 concludes the thesis.

Chapter 2

Fabrication

Micro-fabrication of both pixel-less and pixelated upconversion devices involves up to seventeen steps, and each step is critical. The quality of each fabrication step will directly effect the performance of whole upconversion devices. In general, the fabrication steps are the same for pixel-less and pixelated devices. However, there are some slight differences regarding etchants of wet etching and the position of back contact deposition due to structural differences between the two devices. The fabrication steps for devices with and without metal mirror(s) are also different, since an upconversion device without metal mirror(s) needs no metal deposition before depositions for organic light emitting diode (OLED) layers, and it needs no a second passivation layer deposition and patterning. This chapter introduces in detail several important fabrication steps regarding the working principles and the reasoning behind choosing certain experimental parameters. Certain differences in fabrication for various devices will also be pointed out for clarification. Additionally, later chapters present more-detailed fabrication orders for specific devices.

2.1 Wafer scribing

Before proceeding to any further steps, a device wafer of the appropriate size needs to be prepared by cutting it from a larger, good quality area of raw wafer.

The size of upconversion device varies depending on the structures. Normally, a working upconversion device layout should contain back contact and top contact areas, as well as the active device area that covers the single large pixel for a pixel-less device or the pixel arrays for a pixelated device. The dimensions of the active area for a 64-by-64 pixelated device is around 11.5 cm a side , and for a 128-by-128 pixelated device is around 14.5 cm a side. The top and back contacts are left on intentionally for future probing to apply bias, and their dimensions are adjusted accordingly depending on the size of active area. Therefore, the device sizes are about 15 cm by 20 cm and 20 cm by 25 cm for a 64-by-64 pixelated device and a 128-by-128 pixelated device, respectively. As for the pixel-less device, the size should be about the same as the previously stated dimensions if it has the same active area (15 cm by 20 cm or 20 cm by 25 cm).

One other important issue for preparing a device wafer is to make sure the active area of the device cut off from the raw wafer has no defects. Due to the complicated processing for wafer epitaxial growth, the original wafers always have some defects or certain spots or areas where the layers are not grown properly on the wafer substrate. Because those natural defects cannot be washed away or shaken off by any wafer cleaning methods, the only way to improve the device quality is to inspect the positions of those defects through a microscope, and try to avoid them when cleaving the device from the whole raw wafer. Sometimes, it is hard to find an area that is without defects, and also meets our size requirements. For those cases, one must try to cleave the device from the sample in such way that the defect lies outside the active area. If that is not possible, one must try to

position the defect at the edge of the active area. Briefly, defects must be excluded from the centre of a device's active area.

2.2 Wafer surface cleaning

Wafer cleaning is very critical among all the other steps because it is the preparation before any processing steps; therefore, it directly determines the quality of device's performance in general in future steps. The wafer surface needs to be cleaned thoroughly multiple times until the surface become spotless enough for patterning by photolithography. Otherwise, if dust or organic residue are still attached to the wafer, the photoresist for photolithography cannot be spin-coated evenly on the surface. What makes it worse, is that when the photomask and wafer surface contact during photolithography, the bump caused by those residues may lead to scratches on the photoresist layer, and those scratches will directly result in weak protection for the area supposed to be covered during later wet etching.

The procedure for wafer surface cleaning is as follows. The wafer is dipped into acetone at 40° Celsius for five minute, and then it is dipped into isopropanol at 85° Celsius for five minute. Acetone dipping is used to dissolve most of the organic residues, while the isopropanol dip is used to dissolve the acetone and other organic materials remained on the wafer surface. In general, increasing the temperature is helpful in improving the dissolving performance of acetone and isopropanol, and so has been set as one of the cleaning routines in most laboratories. However, it must be noted that acetone will evaporate at higher temperature and its inhalation is harmful. Therefore, it is advisable to put on a fume hood while dealing with acetone, and not to increase the temperature of acetone too much. After those two steps, the wafer is immediately rinsed with deionized water to wash away the isopropanol. Theoretically, the isopropanol on the wafer surface will automatically

evaporate into the air by itself. The water rinsing is to rapidly illuminate the isopropanol. The reason for using deionized water is to avoid any future interference from the ions existing in tap water. The wafer's surface is examined with a microscope. Sometime during the the inspection, dust can be found still attached to the surface, which indicates that it cannot be washed away merely with acetone and isopropanol dipping. In that case, the cleaning procedures will be repeated, and ultrasonic cleaning may be applied during acetone and isopropanol dipping. The vibration caused by the ultrasound will be able to shake off most of the dust that originally stuck to the wafer surface. The ultrasound power level is set to at most level 3 with the system in the Giga-2-Nano laboratory so that the vibration will not break the fragile wafer.

The wafer cleaning process will be repeated over and over until all the dust and organic residues have been washed away, having an extremely clean wafer for further steps. Ideally, the wafer should be spotless after the cleaning process, yet there are always some defects on the surface brought by the wafer's epitaxial growth process.

2.3 Photolithography - mesa and window patterning

Photolithography processing is used to create patterns on semiconductor devices, and it is therefore used for patterning a mesa structure for the optical upconverters. The photolithography mainly includes three separate steps: spin coating, exposure, and developing.

As soon as the device has been cleaned thoroughly, it needs to be spin coated with photoresist immediately in order to protect the clean surface from any dust in the air. For the first photolithography, AZ3312 photoresist is used for the patterning. AZ3312 is one of the most common positive photoresists used in the laboratory. The normal thickness for AZ3312 is about 1 μm at a spin speed of 4000 rpm for 1 minute, which is good for

this particular purpose because 1 μm is thick enough to protect the areas that are not supposed to be etched during wet etching, and the thickness is also suitable for the 50-100 μm pattern feature size. The final spin coating speed is set to 500 rpm for 10 seconds, and then 3000 rpm for 60 seconds. The 10 seconds at lower speed is a buffer step to make sure the system has a stable spinning at 3000 rpm later. The choice of a spinning speed at 3000 rpm rather than 4000 rpm is to secure the device on the rotation adaptor during spin coating: considering the upconversion device is usually too light and too small to be fixed as good as the larger wafers in the spin coating system, the spinning speed is adjusted down to 3000 rpm. With the given spin coating profile, multiple characterizations has done for the spin coating system, and it seems the customized spinning profile can also gives a 1 μm thickness of photoresist.

After the device is spin coated with AZ3312, the wafer needs to be soft baked at 90° Celsius with a vacuum for one minute. The baking makes the photoresist hard, and turns it from a colloid into a solid. The purpose of the baking is first to make the photoresist hard enough and ready to be molded into certain shapes through future developing, and second to make the photoresist less adhesive and to avoid sticking with the photomask during photolithographic alignment. However, baking the photoresist too long or at too high a temperature will cause it to lose its original chemical properties. It will then not react with light and developer anymore. During the baking process, the vacuum is usually turned on, which also helps photoresist becomes hard more efficiently.

Normally, the next step for photolithography is to align the spin-coated device wafer with the specially designed mask. Due to the fact it is the first photolithography, there is no previous pattern on the device wafer, so there is nothing to be aligned. However, when putting the wafer on the stage, the mesa pattern should be located at center of the the wafer so that there is enough edge space for depositing bottom contact when necessary,

and to avoid the natural defects on the wafer if possible.

The parameters for photolithography are critical to achieve clear features for the device wafer. The most important parameters are exposure time and contact type. If the exposure time is too short, the photoresist will not have enough time to be fully reacted with light. If the exposure is too long, the light may react with the edge of the mesa pattern and result in a ragged pattern edge. As a result of several characterizations for photolithography, the exposure time is set to 6.5s. The contact type is chosen to be soft contact so that the photomask will contact with the wafer to secure the clear features yet will not apply too much force onto the photoresist.

After the wafer bearing with photoresist is exposed to light, it is developed with MIF300 for 20 to 30 seconds with agitation. Agitating the sample wafer during development will help the photoresist develop more evenly across the entire wafer surface. When the wafer is finished developing it is rinsed with deionized water and blown dry gently with a nitrogen gun.

Following development of photoresist is the feature inspection. There are two things to be confirmed: the positions of defects relative to the mesa pattern, and the quality of the features. If the defect is located in the center of mesa pattern, or if the photoresist is peeled off at some places due to over-developing, the wafer needs to go through the cleaning process and plasma ash process to restart the photolithography, until satisfying features are obtained.

The last step for the entire photolithography process is the hard bake. The wafer is put onto the baker and baked at 120 $^\circ$ Celsius with vacuum for one minute. Hard baking the sample after is to completely harden the mesa pattern so that it will not be easily deformed in future processing. The hardened photoresist is also helpful to protect the covered area

during wet etching from etchants.

2.4 Wet etching - mesa etching and window opening

The wafer for the upconversion device is made of InGaAs and InP. It is critical to find a way to selective etch InGaAs without etching InP or vice versa when creating mesas.

The piranha solution is a mixture of sulfuric acid and hydrogen peroxide, which is able to selectively etch InGaAs from InP. Considering the control of etch rate, the piranha solution used for this device is made of sulfuric acid, hydrogen peroxide and water with ratio 1:8:160. Such a solution is dangerous because it is an explosive hazard if not handled properly, in addition to be corrosive, so one needs to be extremely careful when preparing the solution. The correct order begins with deionized water first, then hydrogen peroxide, ending with sulfuric acid. The etch rate for this solution is 350 nm per minute. For the heterojunction photo-transistor (HPT) wafer, it takes around 5 minute to etch 1500 nm of InGaAs. After using the piranha etch, the solution must not be stored in a capped bottle because the bottle may explode due to the oxygen released by hydrogen peroxide. The solution has to be neutralized with potassium hydroxide.

The mixture of phosphoric acid and hydrochloric acid is used to selectively etch InP from InGaAs. The solution is made of phosphoric acid and hydrochloric acid with ratio 10:1 so that the etching rate is controlled at about 300 nm per minute. In practice, it usually takes 30 to 40 seconds to etch 200 nm InP from the heterojunction photo-transistor wafer.

In addition to mesa etching, wet etching is also needed for opening the silicon nitride window for the upconversion devices. For etching silicon nitride, buffered hydrofluoric acid (BHF) is used. The etching rate for BHF is so rapid that it only takes 2 seconds to etch

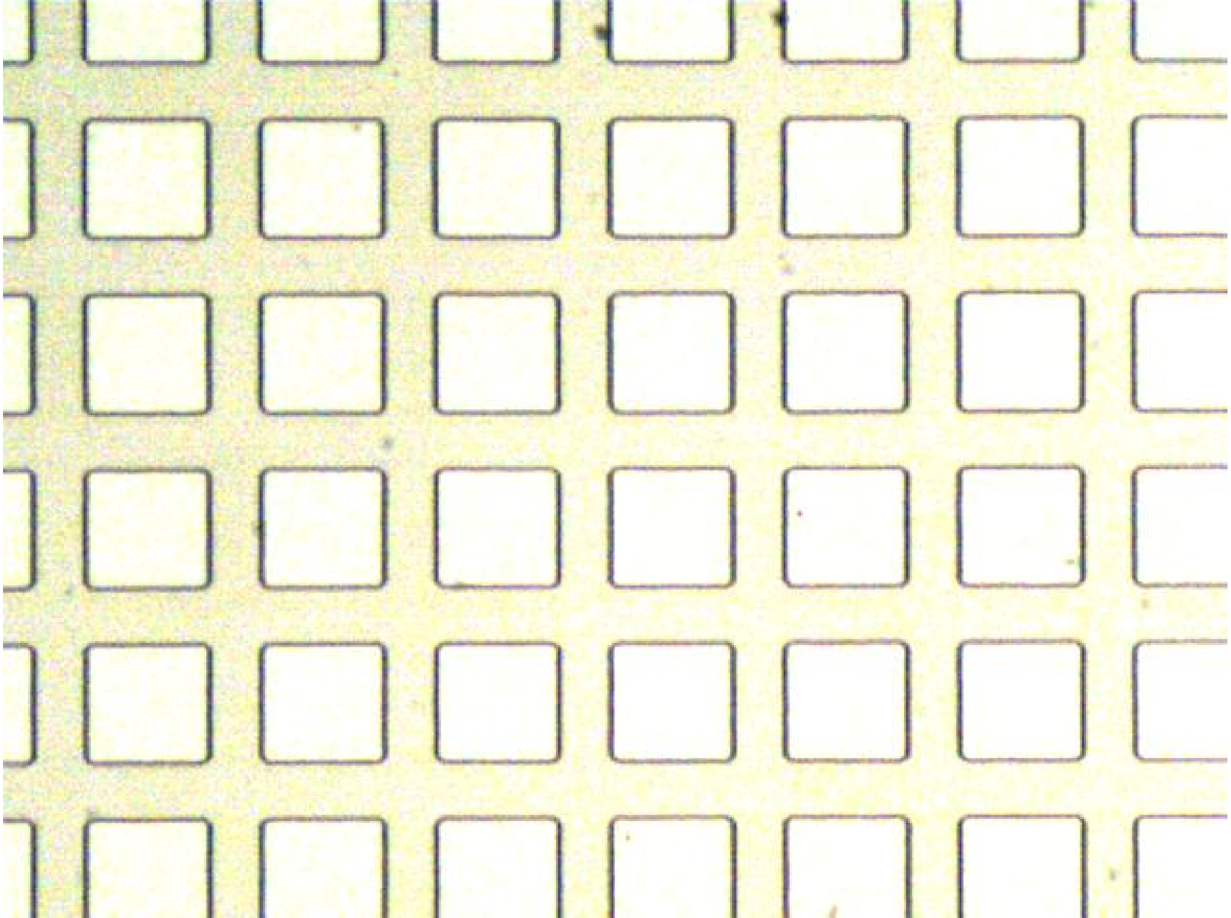

Figure 2.1: Mesas of a upconversion after etching InP and InGaAs layers after 1st photolithography.

through 200 nm silicon nitride. Because of the rapid etch rate, the silicon nitride may not be etched evenly across the whole surface. Therefore, in order to lower the etching rate and control the etching process, BHF solution is further diluted so that it takes 15 seconds to etch through 200nm silicon nitride. Agitation during etching will also be able to improve the etching uniformity.

2.5 Deposition - silicon nitride, metal contact/metal mirror, and organic layers

In fabricating the upconversion device, one crucial part is the deposition. Except for the original structure for the photodetector wafer, all the layers are deposited later during the fabrication, including the silicon nitride insulating layer, metal contact and metal mirror, and the entire OLED layers.

Silicon nitride layer is deposited by Plasma-therm in G2N. The Plasma-therm is a top-down plasma-enhanced chemical vapor deposition (PECVD) device. The working principle for PECVD is to deposit thin film from a gas state to a solid state on the wafer by creating a plasma of the reacting gases with a radio frequency (RF) at 13.56MHz, so that the chemical reactions can take place at such low temperature as 300° Celsius due to the high energy of the gas molecules brought by the plasma. Comparing with other PECVD methods, Plasma-therm is capable of depositing layers in a top-down direction. Because the device wafer for upconversion device is usually very light and small, it is very difficult to hang the wafer upside down to do bottom-up deposition. Moreover, hanging the device may require covering part of the wafer area, which may cause a non-uniform deposition for the thin film in the centre area of the device. For the top-down PECVD, the device

sample simply lies on the stage, and the deposition is more uniform because the entire wafer surface is exposed to the plasma during deposition. After the deposition, the silicon nitride is inspected under microscope regarding its uniformity. If the silicon nitride is not of a good quality, the deposited layer should be etched off using BHF and reattempted.

The metal contact and metal mirror are deposited through evaporative physical vapour deposition. During the process, the source material is subjected to a high current in vacuum, and it is heated from solid state into gas state. The gas state metal then travels through the chamber and reach the surface of device substrate. In the end the gas condense at the surface and turns back into the solid state to form a thin film. The lift-off process is also very important part of the metal mirror deposition. Because the metal mirror needs to be deposited into the silicon nitride windows for each mesa, it is impossible to manually confine the deposition area with tape. Metal lift-off is performed by taking advantage of the previous developed photoresist, depositing the metal onto the entire wafer surface, with only the open area not covered by photoresist will be attached with the metal in the end; all the metal deposited onto photoresist will be lifted off through later dissolving photoresist in acetone. To do the lift-off, the device is dipped into acetone after metal mirror deposition. In the meantime, ultrasonic vibration is applied to help gently shake off the photoresist as well as the metal on top of it. The power for the ultrasonic system should be turned to zero; otherwise it is very likely some metal mirrors will also be shaken off along with the excess metal film.

The entire OLED layers and top metal contact are all deposited through evaporation process in a Kurt J. Lesker OLED cluster tool (FIG. 2.3), which is capable of plasma treatment, sputtering, and evaporation of organic and metallic layers. After putting the device wafer inside the chamber, all processes take place *in situ* by transferring the up-conversion device between chambers for different depositions. The entire connected cluster

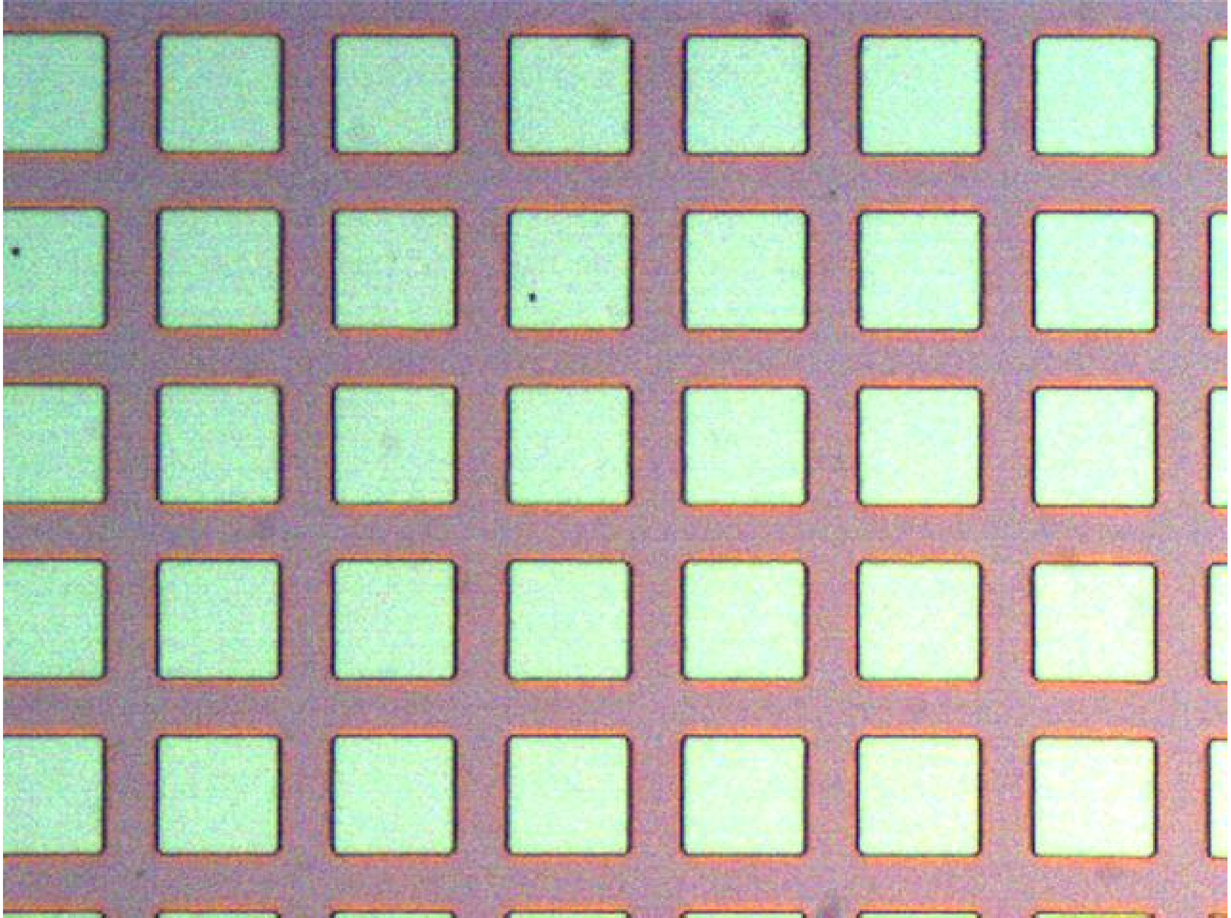

Figure 2.2: Mesas of a upconversion device deposited with silicon nitride insulating layer 1st wet etching.

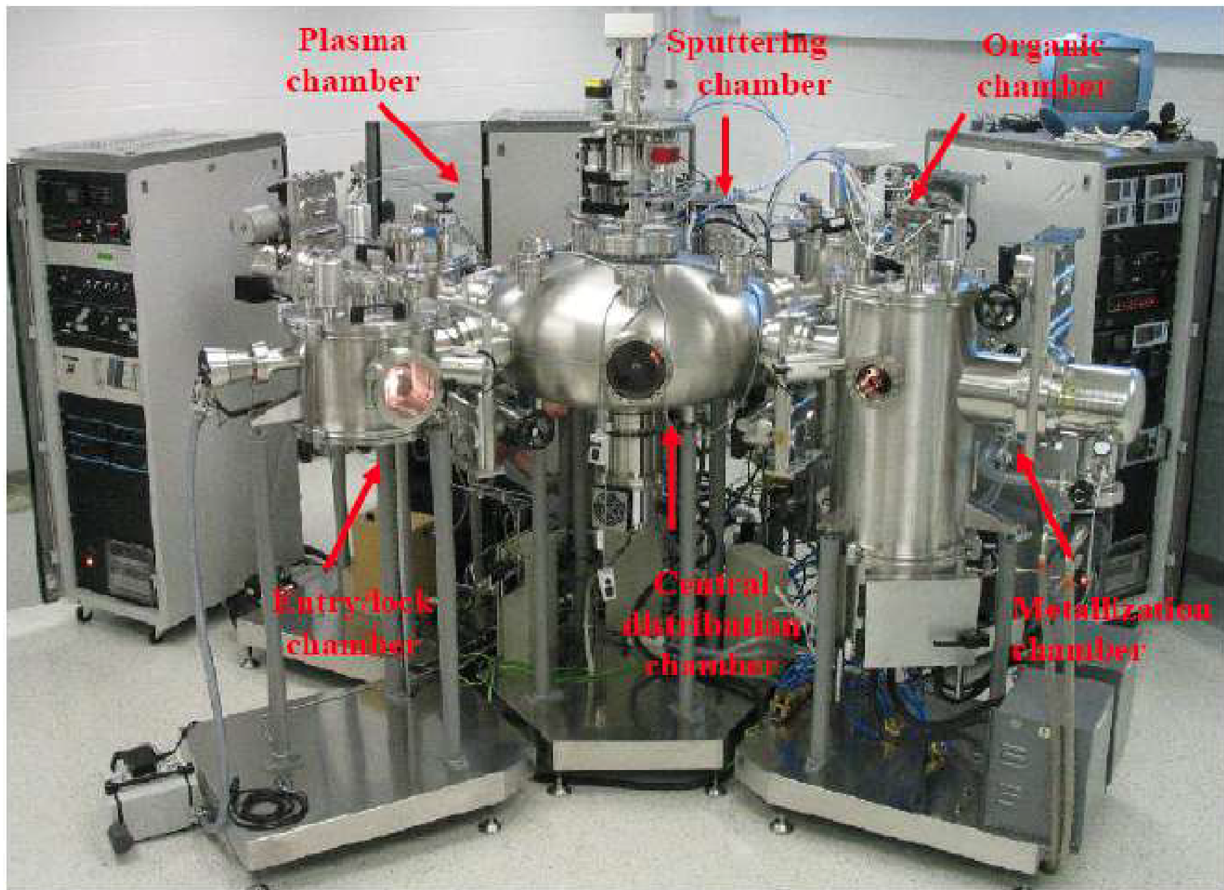

Figure 2.3: A Kurt J.Lesker OLED cluster tool with six chambers[24]

can provide a base pressure as low as $10^{-}8$ Torr. The alignment of the shadow mask and device sample is one of the most important steps during this process. Due to the small size of wafer, the tolerance for positioning of each layer is very small, which makes it very difficult to align the mask and device properly. Moreover, the difficulties in alignment also make it virtually impossible to align multiple devices. Therefore, for each run, only one device can be deposited. As a result, considering the alignment difficulties, several customized shadow masks are designed for different layers (FIG. 2.4). With the assistance of the masks, there is no need for manual alignment with low accuracy, and by using two different narrow glass plates to hold two devices, aligning one device will not affect the other, which allows deposition of two devices in one run with much higher accuracy.

Figure 2.4: Designed mask for cathode deposition mounted onto the sample holder

Chapter 3

Pixel-less Imaging Device

3.1 Motivation

The infrared imaging device has attracted more and more attention due to its wide applications in night vision, homeland security, and semiconductor wafer inspection. The current industrial infrared imaging technology involves combining the commonly used silicon readout integrated circuit (ROIC) and a two-dimensional infrared photodetector array. Because the material used for near infrared detectors is incompatible with silicon ROIC processing, the detector chip and ROIC chip have to be connected with pixel-to-pixel correspondence using indium bumping technology. Therefore, there are several major disadvantages about this imaging technology due to it's device structure: 1) fabrication-wise, it is a one-piece-a-time process because the complicated procedures for pixel-to-pixel indium bumping; 2) size-wise, the device cannot be scaled down due to limitations brought by the high density of indium bumping between the two chips; 3) performance-wise, the indium bumping of each pixel between two chips increases the power consumption and increases the noise

of the electric signal passing through each pixel. To overcome those disadvantages, up-conversion devices that up-convert infrared light to visible light have been proposed and developed for several years. The up-converted light can be directly captured by normal commercial silicon CCD or CMOS with a cutoff wavelength of 1 μm. Therefore, ideally, an infrared camera can be created simply by putting an upconversion device in front of the conventional sensor array inside a normal camera body. To date, several different kinds of upconversion devices have been developed, including thermally excited upconversion devices, rare-earth upconversion devices, photodetector-LED upconversion devices, etc.

Among all the different upconversion device architectures, the photodetector-LED up-conversion devices have been studied and tried for many years due to their simple structures and high working performances. To date, the best performance has been achieved by Chen et al. in 2010, with his inorganic/organic hybrid upconversion device, which is made by depositing an organic light-emitting diode directly on top of an InGaAs/InP heterojuction phototransistor. This device introduced a gain of photocurrent and therefore enhanced the overall upconversion efficiency to over 100%. In addition, the hybrid design takes advantage of both the high quantum efficiency of inorganic semiconductors for detection at infrared range, and the easy and low cost processing as well as the high quantum efficiency for light emitting in the visible range of organic semiconductors. The structure of the photodetector-LED hybrid upconversion device also enables the capability of independently tuning the emitting wavelength of OLED by introducing different organic emitters, and expanding the photo-detection range from NIR to MIR or even FIR by adopting suitable inorganic photodetector designs. Although Chen's device improved the upconversion efficiency to a new level, the heavily p-doped interconnecting layer between the NIR PD and OLED disqualifies it from being a pixelless imaging device. The infrared imaging requires a spatial correlation between the input infrared scene and the output visible light pattern.

However, the upconversion device with its heavily doped interconnecting layer has a severe issue of lateral carrier diffusion that makes it impossible to achieve an up-converted image with high resolution.

Despite low efficiencies compared with hybrid devices, the inorganic pixelless upconversion imaging devices have been demonstrated during the past a few years. The first pixelless MIR upconversion imaging was achieved in 1997 with an inorganic structure integrating a p-type QWIP and a LED, which is able to capture a 1000K hot object[**?**]. After that, in 2004, H. Luo et al. demonstrated the first NIR upconversion imaging. Luo implemented a three-layer structure (undoped-doped-undoped) in the common region between the photodetector and the LED, which ensured the suppression of lateral carrier diffusion as well as efficient electrical interconnection. He also demonstrated the NIR upconversion imaging by using wafer fusion to connect the PD and the LED. Although both of his devices showed the capability of up-converting an infrared scene to a recognizable visible pattern, their efficiencies is extremely low compared with the industrial standards.[46, 9]

Considering the great potential of achieving efficient upconversion device with hybrid structure, and there is no current hybrid upconversion imaging device, a hybrid near infrared pixelless upconversion imaging device was proposed and fabricated by Jun Chen, and it was then characterized by Chen and me through the newly designed imaging measurement system. In the end a real time upconversion imaging was achieved.

The hybrid near-infrared pixelless upconversion imaging device is an integration of a photodetector part and a OLED part. Compared with pervious devices, this imaging device has its absorption layer of intrinsic InGaAs directly in contact with an organic C_{60} layer to form a hybrid junction in order achieve both the photovoltaic effect and the suppression of lateral-diffusion current. The photo-induced electron/hole pairs are generated at the intrinsic layer by the incoming infrared light and the holes separated from electrons go

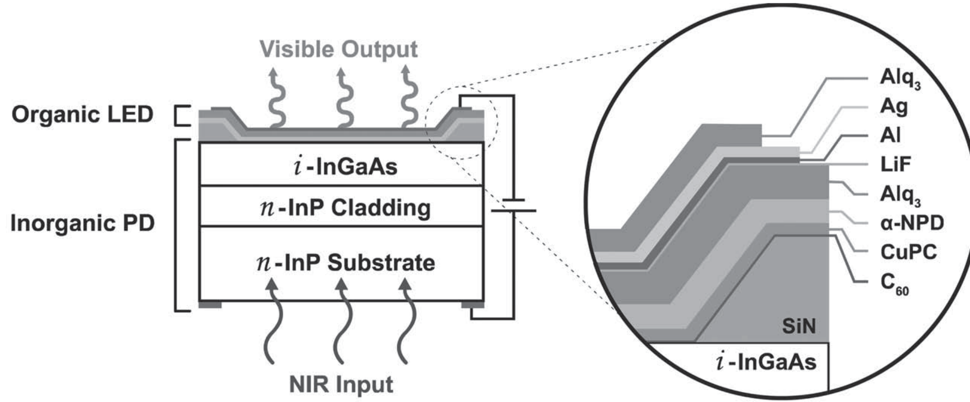

Figure 3.1: (a)Schematic cross-section of inorganic-organic upconverter device. Layer thickness is not to scale: C_{60} is carbon fullerene. CuPc stands for copper phtalocyanine. NPB is N,N0-di(naphthalene-1-y1)-N,N'-diphenyl-benzidine, Alq is tris-(8-hydroxyquinoline) aluminium. Alq:C545T is light emission layer. (b) Schematic band diagram across the interface[20]

through the junction layers to light up a spatially correlated visible pattern across the green-fluorescent OLED layers. The visible green pattern is then collected by a digital camera, and therefore, the upconversion device achieves real-time imaging.

FIG. 3.1 shows a schematic cross section for this hybrid pixelless upconversion imaging device. An n-type InP cladding layer and a $1\mu m$-thick intrinsic InGaAs absorption layer were grown onto a n-type InP substrate sequentially via metal organic chemical vapor deposition (MOCVD). A large area (4mm by 4mm) is confined by an window-like opening surrounded by a covering 200nm-thick insulating silicon nitride layer. On top of that, a C_{60} layer and a green-fluorescent tris-(8-hydroxy-quinolinato)aluminum (Alq_3) OLED are deposited by physical vapor deposition (PVD). The extra C_{60} layer is introduced at the interface of inorganic and organic layers in order to improve the stability of interconnection

between the inorganic part and organic part, and to help the carriers efficiently reaching the OLED layers across the hybrid junction.

3.2 Device fabrication

FIG. 3.2 is the flow chart for the fabrication steps of our pixelless upconversion imaging device. Firstly, a 1-μm-thick intrinsic InGaAs layer along with an n-type InP cladding layer are grown onto an n-type InP substrate by metal organic chemical vapor deposition (MOCVD). The second step was to deposit a 200-nm-thick insulating silicon nitride layer onto the intrinsic layer via plasma enhanced chemical vapor deposition (PECVD). A window of 4mm by 4mm to confine active area of the single large mesa was first patterned by photolithography and then opened by chemically etching through this insulating layer using buffered hydrofluoric acid. After silicon nitride layer deposition and window opening, a special interfacial surface treatment is required before further organic layer depositions. The device was ultrasonically cleaned for 5 min and dipped into chloroform, acetone, and methanol in sequence for 1 min, respectively. The surface of device is then exposed under ultraviolet (UV) ozone for 30 min, during which a sacrificial oxide layer is grown onto the device surface. The sacrificial layer was later etched off in an $(NH_4)_2S$ solution ($25wt.\%$) at room temperature for 5 min. Acetone and methanol dipping are applied again after etching before loading the device sample into a Kurt J. Lesker LUMINOS cluster tool for later depositions[62]. After surface treatment, all depositions are physical vapor deposition and were occurred *in situ* without break the vacuum. OLED molecular layers are first deposited sequentially onto the entire device surface through a shadow mask. The following step is using a second shadow mask to deposit on top of the square mesa the semi-transparent cathode metal layers made of $LiF(1.0nm)/Al(5.0nm)/Ag(15.0nm)$. The

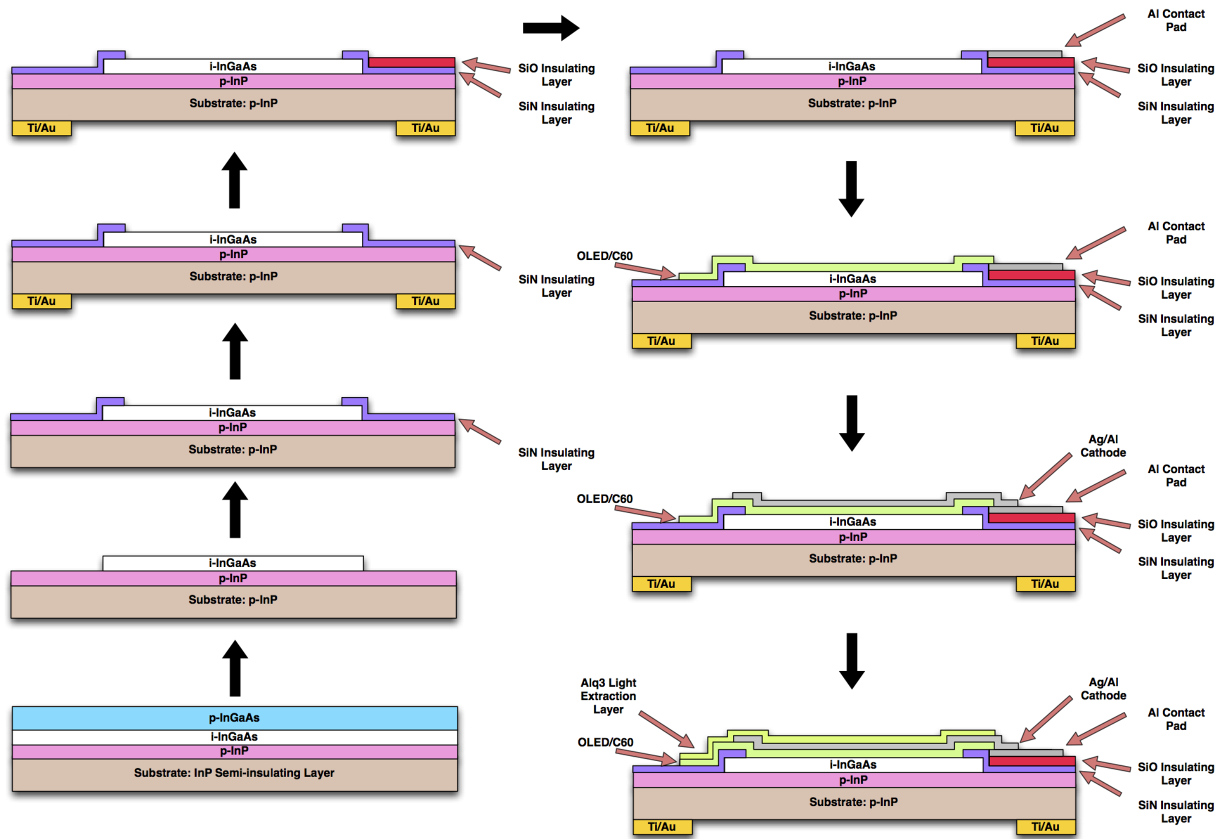

Figure 3.2: Flow chart of fabrication step for the pixelless hybrid imaging upconversion device

cathode layers must be thick enough to provide adequate sheet conductivity while staying partially transparent to green light. The final step is to deposit a Alq_3 light extraction layer with a thickness of 45nm for a better refractive-index matching between air and the cathode layers. Since the substrate is conductive, a glue of liquid InGa is used to connect the backside of the upconversion device with a conductive tape as the back contact. The glued area should not block the area for incoming infrared light[20].

3.3 Working principle

The proposed hybrid pixelless upconversion imaging device consists of one large-area single mesa, which is intended to convert infrared scenes to spatially correlated visible images. Theoretically, photons absorbed in a photodetector (PD) should flow vertically (from PD to OLED) and lateral carrier flow (across the plane perpendicular to incoming light direction) should be forbidden. As a result, only the front area that has its corresponding back area illuminated under infrared light emits green light, and the other area remains dark. Therefore, carrier diffusion needs to be suppressed laterally in order to avoid lighting up the OLED part around the illuminated area, which will severely reduce the resolution of up-converted images. Meanwhile, the device should also preserve efficient electrical connection between the PD and OLED so that the photocurrent is able to trigger the OLED of the area that is illuminated at the back of the device.

To achieve those objectives, the layer structure of hybrid upconversion devices should be carefully designed. Therefore, based on the previous upconversion device integrating a p-i-n photodetector and OLED, Chen modified the photodetector part by removing the p-type layer. In that case, the infrared light illuminates the photodetector side, goes through the substrate and cladding layer, and is eventually absorbed at the i-InGaAs absorption layer due to the photovoltaic effect of $i - InGaAs/C_{60}$ heterojunction, which has been observed also in other similar $inorganic/C_{60}$ hybrid semiconductor junctions[35]. The photon-generated carriers will then directly flow to the organic layers without spreading laterally. Besides the layer structure for the inorganic part, the suppression of lateral carrier diffusion also strongly depends on the conductivity of the organic layers. Because the mobility of carriers in organic materials is relatively poor and the thickness of each organic layer is very thin, the conductivity across the large mesa area is expected to be very

low. Therefore, lateral carrier diffusion across the organic layers is so trivial that it does not effect the quality of an up-converted image[37, 51]. Simulations have been done by Jun to study the lateral diffusion effect of such upconversion device structures. The results showed carrier lateral diffusion that was suppressed efficiently, and the carrier spreading of this structure was mainly controlled by absorption layer thickness, regardless of the input power of infrared light[16].

The structure of this newly proposed hybrid pixelless upconversion imaging device also has a benefit of simple fabrication. With only one large-area mesa, the uniformity of the device's surface is more easily controlled compared with the devices with a mesa array. Moreover, with only one layer to be patterned and etched, there are fewer fabrication steps compared with other devices, such as HPT-OLED upconversion devices. Therefore, there are less fabrication factors involved during device processing, which indicates a better-quality upconversion device.

To verify the performance of this modified structure of an upconversion device, Chen fabricated such upconversion device with a single small-area mesa ($0.8 by 0.8 mm^2$). The photovoltaic effect of the $i - InGaAs/C_{60}$ Schottky junction was confirmed during the characterization of this device, and the device gave an overall upconversion efficiency of 0.4% W/W at 24V, with an input optical power of 1 mW/mm^2.

3.4 Imaging measurement system

The imaging measurement system is designed to measure the L-I-V characteristics of an upconversion device and to capture the up-converted image clearly. The system includes a laser system, optical alignment configuration, camera system, and the measurement units. FIG. 3.3 shows the entire system. The laser system outputs infrared light at a wavelength

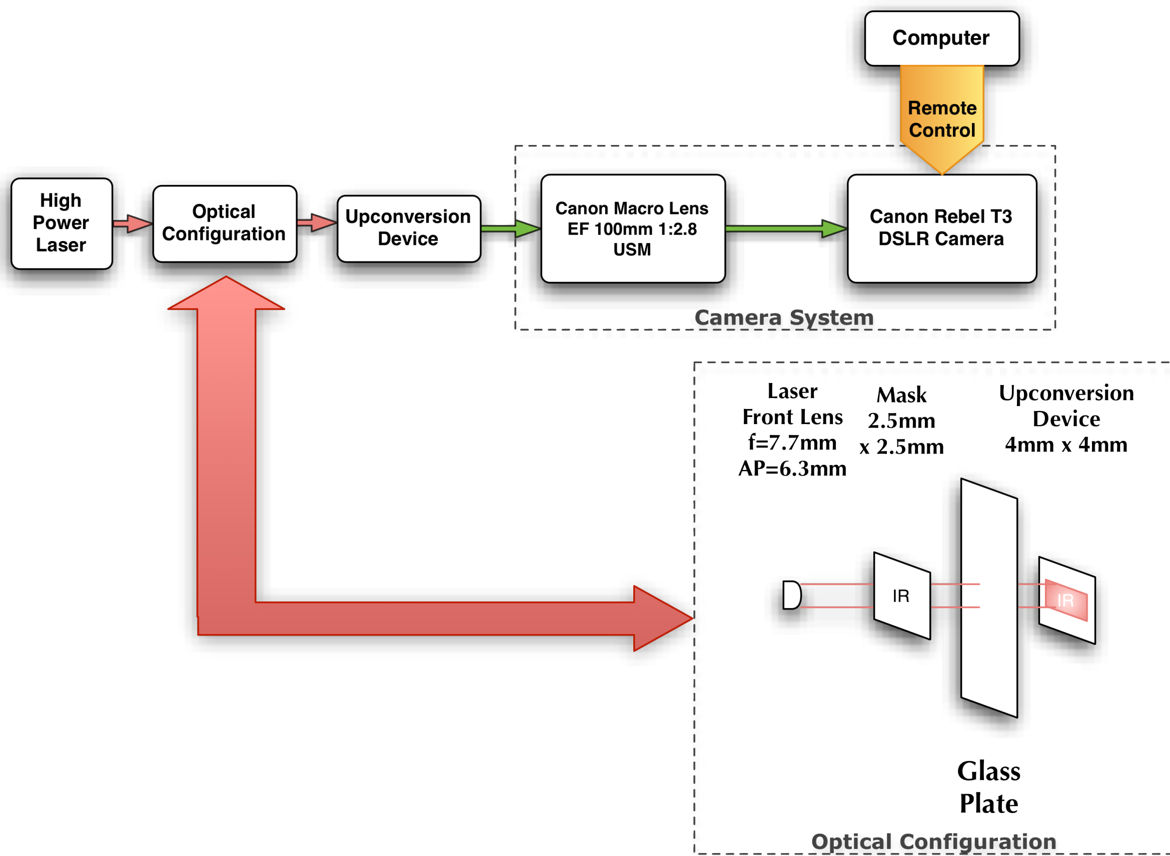

Figure 3.3: The designed characterization system for the imaging upconversion devices.

of 1.55 μm, and the light passes through mask and reaches the back of a upconversion device. The up-converted pattern at the front side of an upconversion device is captured by the camera system. The upconversion device is driven by a 4140B PA Meter/DC Voltage Source, which can also monitor and record the current flowing through the device in real time. The camera system can be replaced by a Minolta luminance meter, which is connected with the voltage source so that an L-V curve can be recorded.

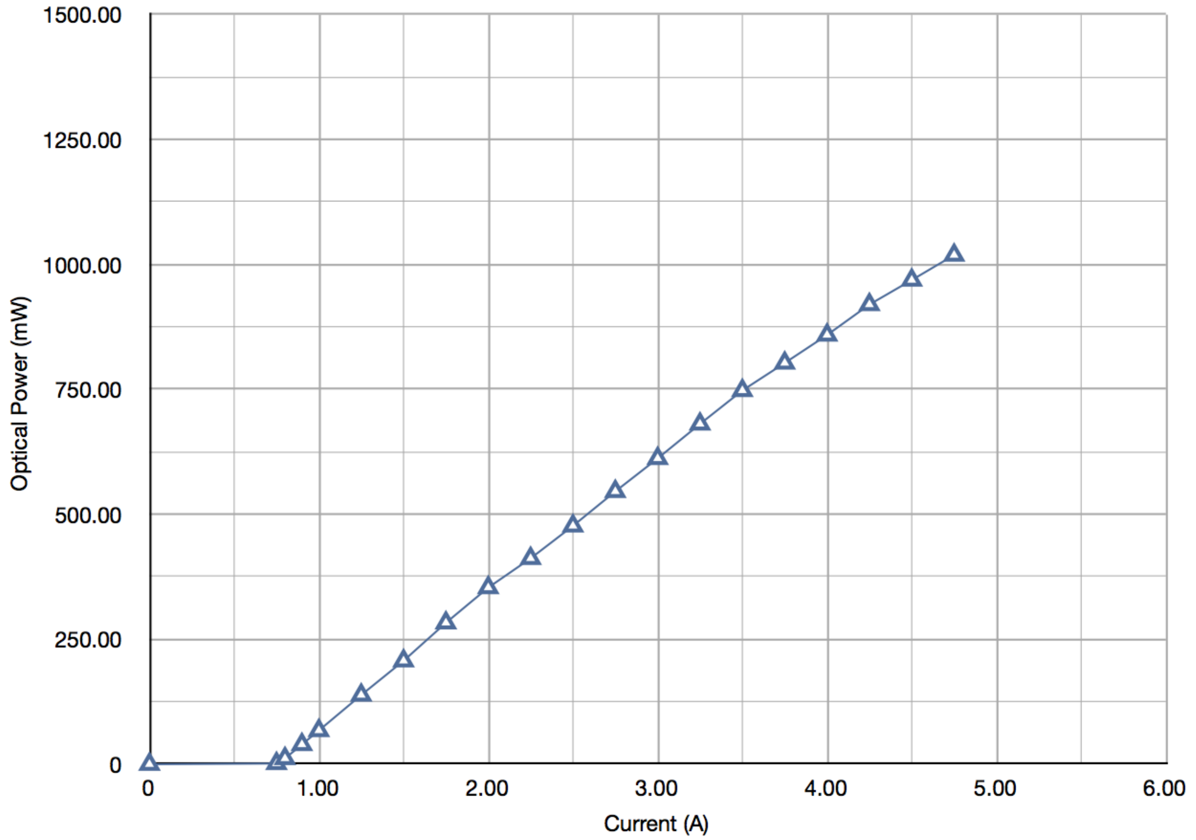

Figure 3.4: Characterization results of the high power laser system

3.4.1 Laser system

A SemiNex high-power infrared laser is chosen to serve as the incoming infrared light source. The laser engine can emit infrared light beam at a wavelength of 1.55 μm with a max optical power above 1W. FIG. 3.4 is the characterization results for this laser engine. The highest optical power output is measured to be 1.06W at a bias 7.2V with a current of 5.0A. To drive this high-power infrared laser, a 1 Ohm resistor needs to connect with it in series to protect the laser engine from any current surge during operation.

3.4.2 Alignment

During the imaging measurement, a high power laser, a mask, an upconversion imaging device and a camera with a lens needs to be aligned so that the infrared laser can go through the mask and project to the active area of an imaging device, and the output visible pattern can be captured by the camera system and show at the centre of the recorded image.

FIG. 3.5 shows the setup for the optical alignment. All the components requiring alignment stay on an optical rail, on which each component can adjust the height and the relative distances between each other. The high power laser is located at one end of the optical rail. The laser engine is mounted with a cylindrical lens that collimates the laser beam in vertical direction with a width of about 4mm, yet the laser beam is expanding horizontally. Therefore, the mask is put at a distance away from the laser such that the laser beam profile in the horizontal direction is expanded to be large enough to cover the pattern on the mask. The upconversion device is put on a glass slide held by a device holder, which is located right at the back of the mask. In this way, the laser pattern passing through the mask does not distort too much in the horizontal direction due to its expanding. The tricky part of alignment is to locate the position of the upconversion device relative to the infrared pattern. One way to do this is to mark the location of the device's active area on its mounted glass slide, and mount the glass with the mask onto the glass slide with the device according to the labelled position marks as illustrated in FIG. 3.6. On the other end of the optical rail sits the camera with its lens. The distance between the upconversion device and the camera is adjusted to 31 cm in order to optimize the magnification ratio to 1:1.

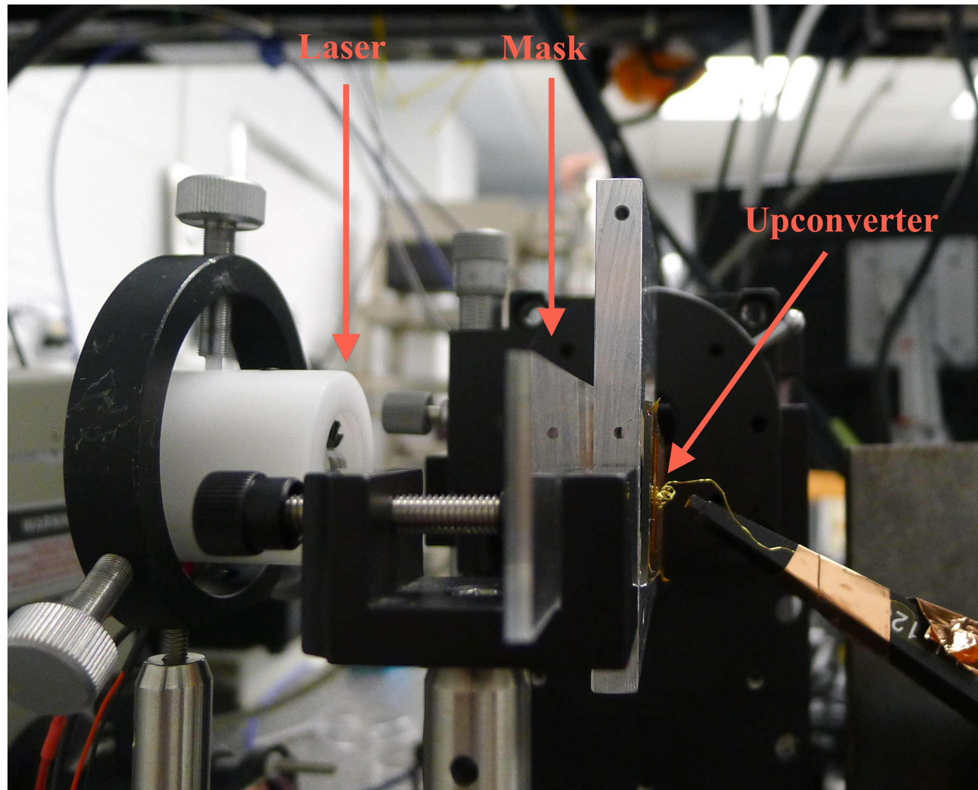

Figure 3.5: The optical alignment configuration for the measurement system of imaging upconversion devices. Note that the mask is put at certain distance away from the laser so that the laser beam can expand and cover the entire letter pattern on the mask. The device is put very close to the mask to avoid a loss of optical power and the distortion of laser pattern due to the laser expansion.

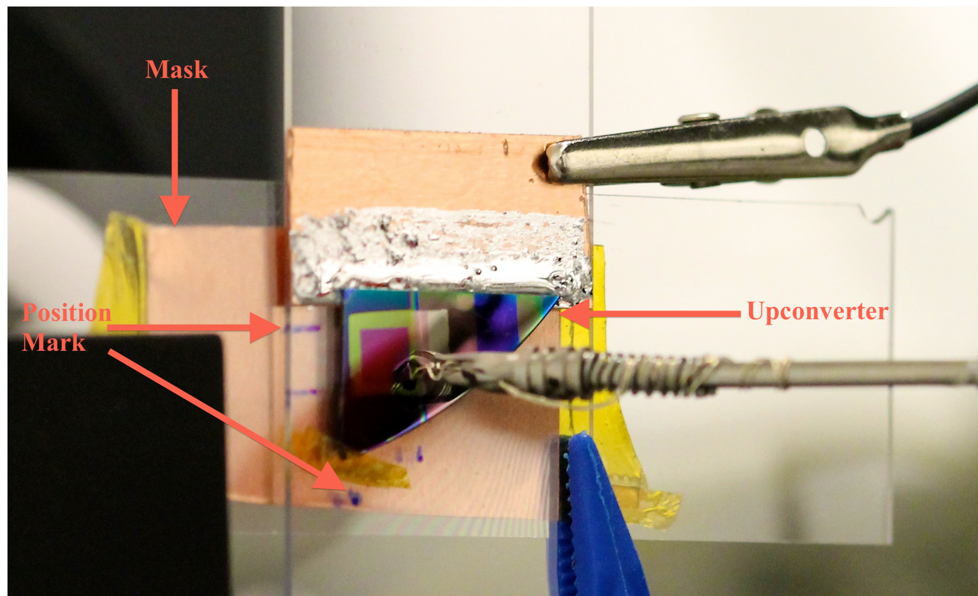

Figure 3.6: The illustration of alignment between the mask and the upconversion device. Position marks are labelled to assist positioning the mask at the back of the upconverter without seeing the actual device's active area.

Figure 3.7: The camera system used in our measurement system of imaging upconversion devices

3.4.3 Camera system

As illustrated in FIG. 3.7, the camera system consists of a camera body along with a special macro lens, and a laptop to digitally control the camera while capturing visible patterns coming out of the front side of a upconversion device. The luminance meter in front of the camera is used to measure upconverter's L-I-V curve, and it will be removed when conducting an imaging test.

A Canon EF 100mm f/2.8 lens was specially chosen for the measurement. The environment is extremely dark during the measurement, and the only light source is the OLED

of the upconversion device. In addition, an upconversion device is usually very small, so the pattern from the device will be even smaller. Therefore, a large aperture macro lens is needed to capture pictures of small objects in dark environments. The lens chosen in the system can focus on the upconversion device at a distance as close as 31cm, with a life-size ($1\times$) magnification. The large aperture of 2.8 at 31cm also helps to capture as much light as possible from the device. However, the large aperture results in a very shallow depth field, which may cause a problem when one trying to focus the camera onto the upconversion device.

The camera used in our imaging measurement is a Canon Rebel T3 digital single-lens reflex camera, which has a 12.2-megapixel CMOS sensor array of 22.2 by 14.7 mm^2. By dividing the sensor array area with the number of sensors, an area of 27 μm^2 can be covered by one pixel. That is to say, each pixel is about $5.2 \times 5.2 \mu m^2$, and with a 1:1 projection of an object, a resolution of $5.2\mu m$ can be achieved theoretically. In real practice, due to the difficulties of focusing under dark environment with large aperture, the focal length was longer than 31cm, which resulted in a smaller magnification ratio hence lower resolution . The camera is connected through a laptop so that it can be controlled remotely by software. The software enables us to adjust shutter speed, aperture, and sensor sensitivity, the ISO, for up-converted pattern shooting. With the right settings, a sharp and clear image can be captured even in dark environments.

3.5 Pixelless Imaging Result

After the verification of performance for a small-area upconversion device with the modified structure, several same-structure devices with a single mesa of size 4 by 4 mm^2 were fabricated for characterization and real-time upconversion imaging tests. Compared with

other upconversion devices, such as the $p-i-nInGaAs/InP/OLED$ upconverter, the interconnection layer of our biased imaging upconverter becomes completely depleted, hence has a very small lateral carrier diffusion current at the inorganic/organic interface. At the same time, the layer also keeps sufficient electrical connection for carrier flowing from the inorganic photodetector to the constituent OLED. Among the fabricated devices, one was successfully characterized by Chen, and the other two devices achieved the real-time imaging of upconversion, with a positive mask and a negative mask, respectively. Among the devices tested for real-time imaging, all were biased at -10 V at room temperature, and with the mask attached at the back of them.

Before our imaging tests, Jun Chen first characterized one device and showed that the designed structure was able to up-convert infrared light with a wavelength of 1.55um to visible light with a wavelength of 520 nm. The L-V curve of this device under an infrared illumination with a power of $6mW/cm^2$ is illustrated in FIG. 3.8. Chen also demonstrated the photovoltaic effect of $In_{0.53}Ga_{0.47}AS/C_{60}$ by measuring the total device current with different infrared optical power input [FIG. 3.9]. One can clearly see the evident device current differences with different input power settings. In the end, the overall external upconversion efficiency of this imaging device is calculated to be $0.57\%W/W$ when biased at 16 V with a $6mW/cm^2$ NIR illumination[15, 20].

During the imaging test, the positive mask was tried first. When the device was biased, the infrared-illuminated letter pattern was up-converted at the front of the device. However, the positive mask (the opening area is the letter) blocks most of the infrared light while allowing a very small amount of light to pass through the letter-shape opening to reach the back of the upconversion device. As illustrated in FIG. 3.10, because the input optical power for the upconversion device was very weak, the front-emitting light of the area illuminated at the back of the device was not bright enough, which resulted in a weak

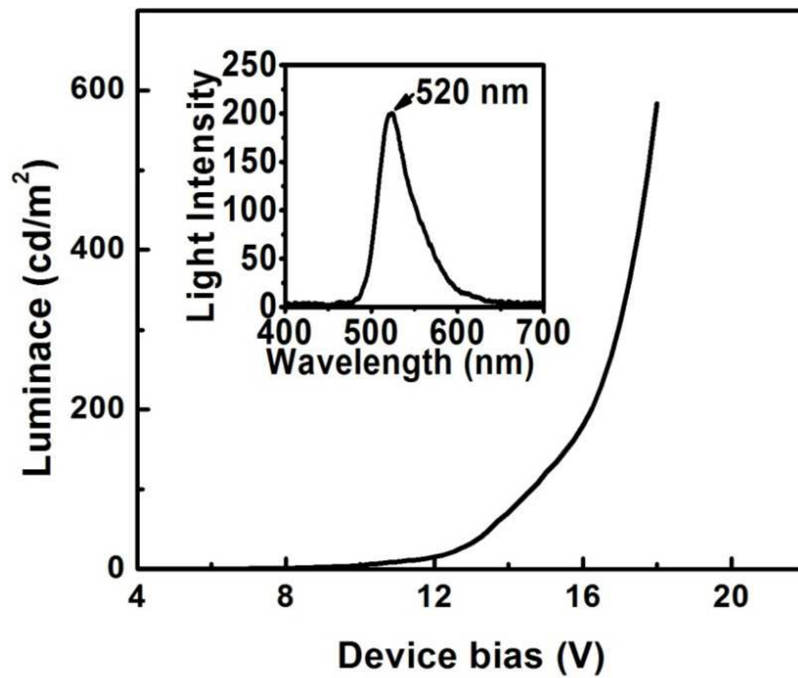

Figure 3.8: Luminance-voltage (L-V) curve of the pixelless imaging upconverter under 1.5μm infrared illumination with $6mW/cm^2$ power [inset: the emission spectrum from the OLED of the integrated upconverter peaked at 520 nm in wavelength (green light)].[15]

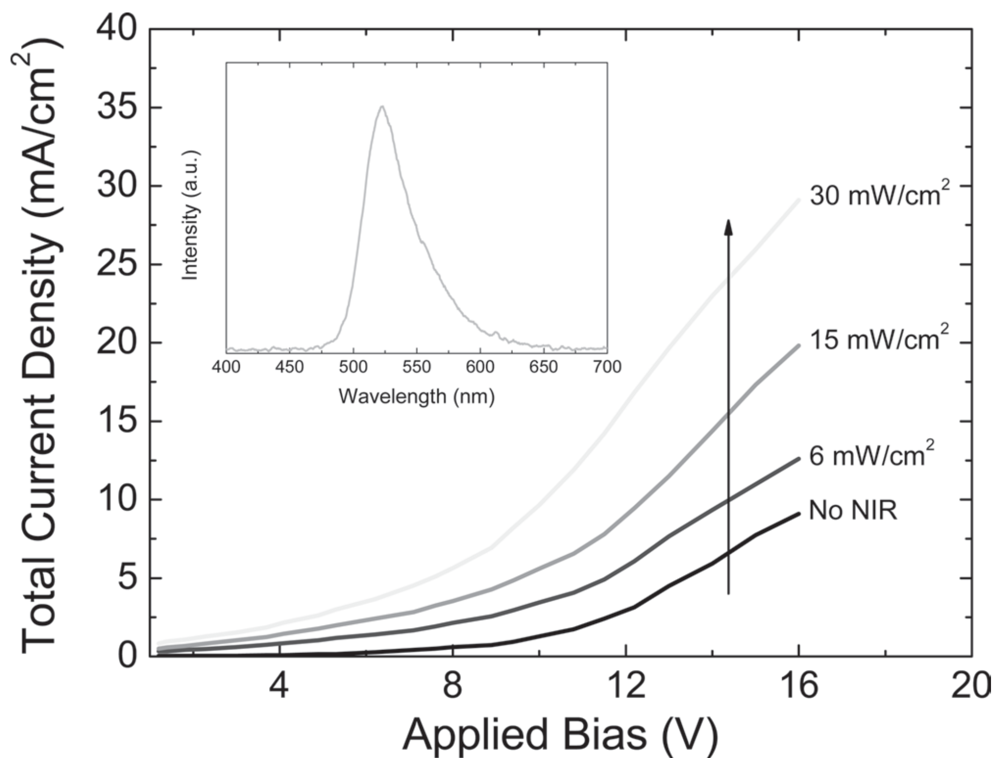

Figure 3.9: The NIR-induced device's current as a function of device's bias under different illumination conditions.[20]

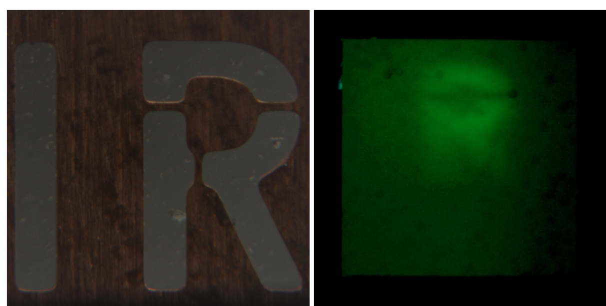

Figure 3.10: The comparison of the used positive mask (left) and the imaging result (right). Only the letter "R" can be recognized, and the edge is very blurry without enough clarity.

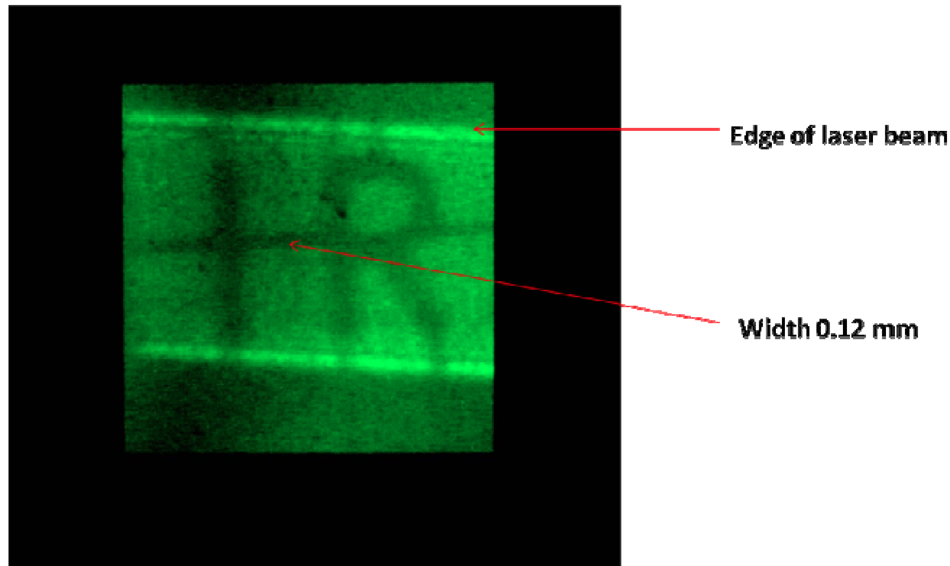

Figure 3.11: The imaging result of the pixelless upconversion device using a negative mask. The linkage part of the letter pattern and the edge of laser beam can be easily recognized with good contrast and clarity.[20]

contrast between the up-converted letter pattern and the surrounding area. Therefore, the imaging with a positive mask is not very satisfying because it is difficult to recognize the up-converted pattern, letter "IR", on the image.

On the other hand, when using the negative mask for upconversion imaging with another device, there is more light coming through the mask and reaching the back of the upconversion device. When the device was under a bias of only 10V at room temperature, the device current had already been capped at 10 mA due to the maximum current flowing allowed by the source. The high device current for this upconversion imaging is mainly because there is more area illuminated by the infrared light, hence, a larger photocurrent is generated by the absorption of optical power. FIG. 3.11 is the imaging result for the hybrid pixelless upconversion device with a negative mask. With a good contrast brought by

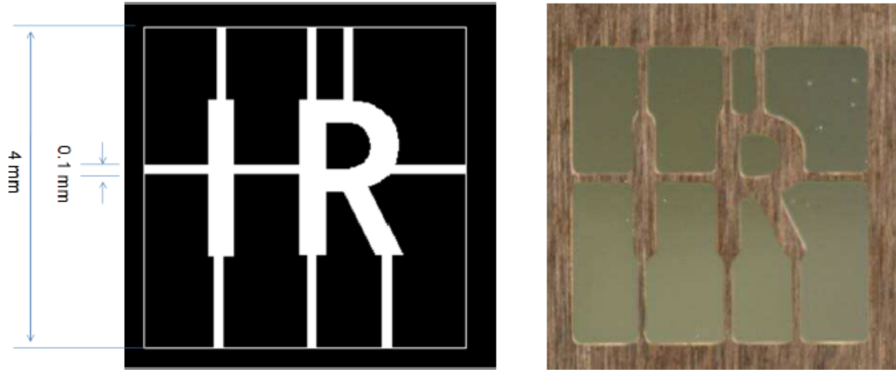

Figure 3.12: The design and the actual photo of the negative mask with letter "IR" pattern.[16]

the bright background, the dark letters "IR" can be clearly recognized in the up-converted image.

The resolution is a very critical factor in judging the performance of an imaging device. The resolution of our hybrid pixelless upconversion device can be measured and calculated by comparing the letter on the mask we used and the up-converted pattern. The negative mask is made of a sheet of brass with a thickness of 0.2mm. FIG. 3.12 shows the letters "IR" on that mask. They have the minimum feature size of 0.1mm, which is the width of the linkage between the two letters. As a comparison, the width of the linkage part on the up-converted image is also measured, and is 0.12 mm. The resolution is therefore calculated to be $10\mu m$ by using the measured width of the linkage part from up-converted image minus the width of the corresponding part from the mask design, and dividing the number by two, considering there are two sides of the linkage. The 10 μm resolution of upconversion is very close to the theoretical resolution of our camera system, 5.2 μm, a finding that indicates that the upconversion resolution may be limited by the camera system[16].

3.6 Conclusion

In this chapter, with Jun Chen's efforts on characterization, the real-time upconversion imaging of the $i - InGaAs/C_{60}/OLED$ hybrid pixelless upconversion imaging device was demonstrated with good contrast, and an imaging measurement system was also designed and set up for the imaging devices. During imaging tests, the $i - InGaAs/C_{60}$ junction was shown to successfully provide a photovoltaic effect for infrared detection, and it was also shown to suppress the lateral carrier diffusion while preserving a good electrical connection at the inorganic/organic interface. The first-ever hybrid upconversion imaging was achieved with a resolution of up to 10 μm. The results show that there are great potentials for this $i - InGaAs/C_{60}$ heterojunction in the application of pixelless NIR imaging.

Chapter 4

Pixel-lated Imaging Device

4.1 Motivation

With the development of the single-element infrared upconverter, the infrared upconversion imaging device has become a possible replacement for the current infrared camera, with potential for higher detection efficiency and resolution. In the previous chapter, a hybrid pixelless upconversion imaging device was introduced, and a successful infrared upconversion was presented, with recognizable up-converted letter patterns. The hybrid architecture combines both advantages from inorganic semiconductors and organic conductors. The inorganic semiconductors normally have higher quantum efficiencies for infrared light detection than those of the organic semiconductors. They also have the capability to expand the photodetecting range from NIR to MIR or even FIR by adopting suitable inorganic photodetector designs. On the other hand, the organic semiconductors now have high quantum efficiencies for visible light emitting, and the emitting wavelength can be tuned by introducing different organic emitters. In addition, the organic materials are

also flexible, cheap, and easily processed. The hybrid upconverter has all those advantages while not being restricted by the disadvantages brought by pure inorganic or organic devices. For example, the hybrid architecture for the upconversion device has an in-out-different-side operation. Limited by structure, an organic upconverter requires that the infrared light enters from the same side as its light is emitted. However, the hybrid device takes advantage of the organic materials while not being restricted by the original organic structural, and it can perform with light incoming and outgoing at different sides. Moreover, the materials used for light emitting are not limited by the lattice constant of the top-most semiconductor layer.

However, although infrared upconversion has been demonstrated with the pixelless upconverter, because of the single-large-area mesa used in the pixelless device, the overall upconversion efficiency has been limited by this device's special designed structure used to suppress lateral carrier diffusion at the interfaces between the photodetector and the OLED. Therefore, the pixellated structure was introduced to potentially improve the resolution of the imaging device without sacrificing the device's high upconversion efficiency. For a pixellated device, because each photodetector is completely independent, the upconverter is more reliable in the sense that one or several dead pixel(s) will not effect the entire device's performance. The pixel array also allows one to achieve any resolution according to one's purpose by adjusting the size of each mesa and the spacing between them, as long as the resolution is within the current or future capability of the fabrication technology. The current technology can provide at least a $8\mu m$ pixel size for a full frame sensor made of 12 mega-pixels, for which we can anticipate that the infrared pixellated upconversion imaging device can achieve the same or higher resolution, ideally.

As shown in FIG. 1.10, the pixellated device was based on Chen's previous design of hybrid single-element infrared upconverter, for which he integrated an p-n-p HPT with a

film of OLED. The amplification brought by the HPT significantly enhanced the responsivity for infrared photo-detection, which gave an upconversion efficiency of $0.07W/W$ for his first HPT/OLED hybrid upconverter. Later Chen further optimized the layer structure of HPT and also introduced the embedded mirror, and his new device achieved the highest ever upconversion efficiency of $1.55W/W$. The proposed pixellated device made use of the optimized HPT structure. However, the embedded mirrors were not used for our pixellated device as the device quality degradation was considered to be due to a more complicated fabrication process and the possible trapping of moisture underneath the metal mirror, which may damage the OLED during later fabrication.

4.2 Device fabrication

The wafer used for fabricating the pixellated imaging upconverter started from an infrared-transparent InP substrate. To realize a structure of p-n-p HPT, the p-type InP layers, an intrinsic InGaAs layer, a n-type InGaAs layer, and the p-type InGaAs layers were epitaxially grown onto the substrate in sequence through molecular beam epitaxy (MBE). The high-low profile mentioned before was introduced here as well by inserting the intrinsic InGaAs layer between the InP emitter and the n-type InGaAs layer, thereby improving the hole-injection efficiency from the emitter into the base.

At certain size, the device was cleaved off from the wafer, and the mesa etching followed: 16384 mesas (128 by 128) were first patterned by photolithography across the device's surface, with a mesa size of $70\mu m$ for both width and length, and with 25 μm for spacing. Then the InGaAs layers at the spacing areas were completely etched off, and the etch stopped at the p-type InP so that the conductive InP layer acted as a common terminal to bias the entire mesa array. A 300 nm-thick insulating layer of SiN was later deposited

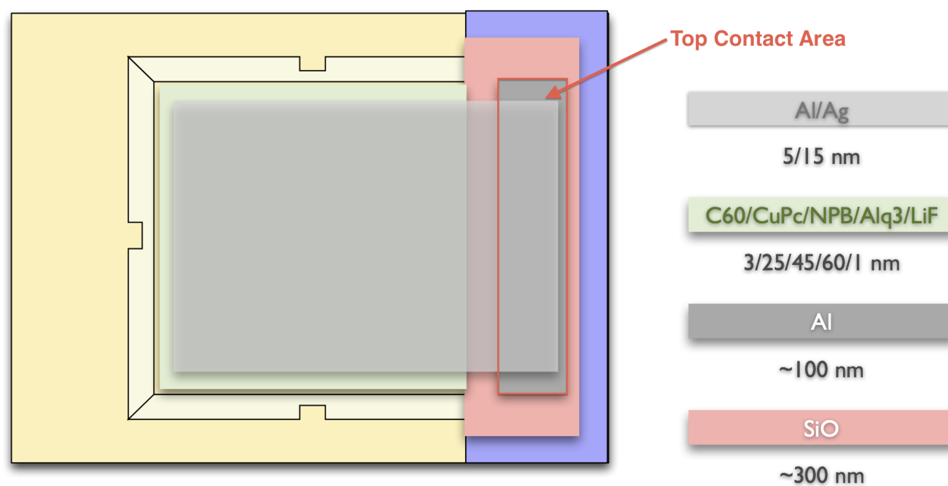

Figure 4.1: Layout of a pixellated hybrid upconversion device. The area confined in the red box is left as top contact pad for probing. Underneath the conducting Al/Ag contact pad, SiN and SiO insulating layers were inserted to avoid short circuit between bottom contact and top contact.

through PECVD at 300 $°C$. The layer was then patterned and window-like openings sized of 45 μm were etched into each mesa. A layer of Ti/Au was deposited onto p-InP in bottom contact area with a very low contact resistance[25, 34]. The OLED layers, which consist of a 3nm layer of C_{60} , a 25 nm layer of $CuPc$, a 45 nm layer of NPB, a 60 nm layer of Alq_3, and a 1 nm layer of LiF, were deposited across the entire mesa-array area *in situ* through evaporation. The cathode, a 5nm layer of Al and a 15nm layer of Ag, were evaporated onto the top of the organic layers later. In the end, an additional organic layer consisting of Alq_3 was deposited on the top the mesa-array area to help extract the emitted light from the imaging device.

The layout of the deposited layers during the device fabrication was carefully designed, and it being extremely important for the device to function properly. Because the pixellated

device has hundreds of devices that need to be biased simultaneously, the cathode for the OLED was deposited as a continuous layer. In addition, in order to protect each mesa from damage when probing to apply device bias, the device wafer had a side area with a top layer of p-type InP for the cathode layer to extend to. In this way, when applying the device bias, the probes contact with the extended contact pad rather than directly touching the device mesa. However, with this method, because now the cathode and anode were all deposited on the same p-type InP layer, extra insulating layers were required and the layout position of each layer needed to be controlled very precisely to avoid the short circuit between the anode and the cathode. As shown in FIG. 4.1, a layer of SiN insulating layer of 300nm thickness was extended from the mesa-array area to the top contact area left for cathode probing. On top of that, another 300nm SiO layer with a smaller area was deposited to secure the insulation, and a 100nm titanium layer was evaporated after as a contact pad to support the extremely thin cathode layer. The titanium contact pad was confined within the area of the SiO layer to avoid any leakage path from the top electrode to the bottom electrode. With all those pre-deposited protection layers underneath, the OLED cathode layer was deposited in the end to bridge the mesa-array area and the contact pad so that all mesas were able to be biased by probing the contact pad.

4.3 Pixellated imaging results

The imaging device remained dark, with a normal bias around $20V$. By increasing the bias, the pixels at the edge started to light up at a bias around $40V$ without any incoming infrared light, and by pumping up the bias, more pixels were lit up, but a large area of pixels at the center of device still remained dark (FIG. 4.2).

To test the upconversion of the imaging device, the laser was placed right at the back

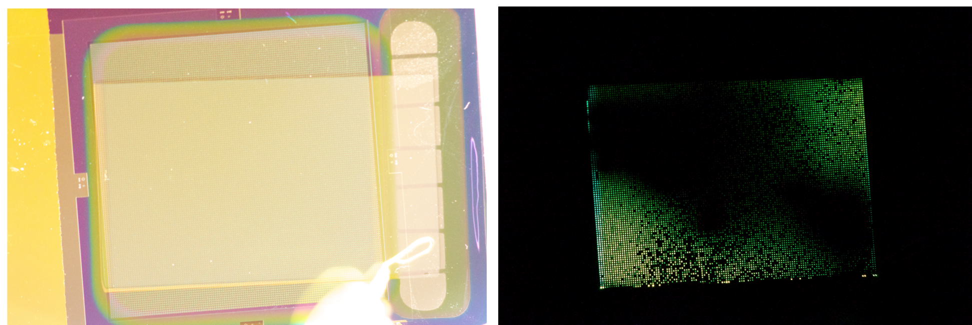

Figure 4.2: Photo of the pixellated hybrid upconversion device. It was taken when the device was biased around 40V. The central area was dark indicates the pixels there were not working properly.

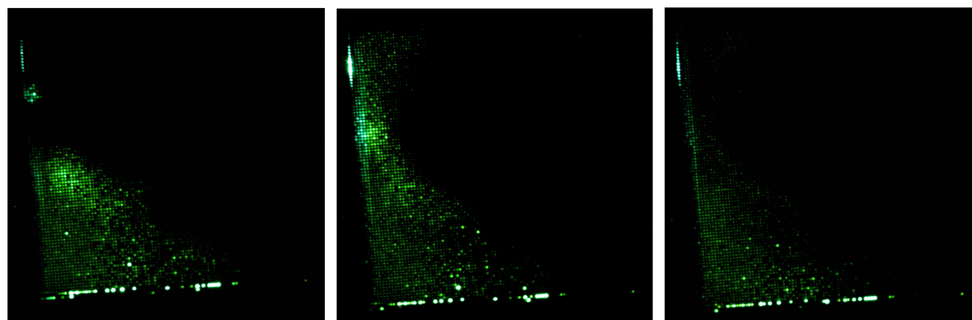

Figure 4.3: Imaging results when the high power laser was directly placed at the back of the pixellated upconverter (left), when the laser moved (middle), and when the laser was blocked (right)

of it. When the laser, at a power of $300mW$, was turned on, however, the central area did not light up when the laser was in central position at the back of the device. The laser was moved to the edge area where the pixels were working, and the upconversion device showed a recognizably brighter pattern at the corresponding position of the laser at the back. When the vertical and horizontal position of the laser were gradually adjusted, the pattern moved accordingly. Finally, the laser was blocked by a black card, and the brighter pattern of the upconverter disappeared. FIG. 4.3 shows the imaging results.

The next step was to see whether the upconversion imaging device was able to image certain projected infrared patterns at the back. Therefore, we put a specially designed mask in front of the laser, at certain distance, so that the laser beam could expand large enough to cover the letter on the mask. The upconversion device was put close in front of the mask to avoid the loss of optical power of the passing infrared light. Unfortunately, the pattern was not recognized during experiments, either because of mis-alignment caused by laser position adjustment or the lower optical power for the amount of infrared light passing through the mask.

The mask was then removed again for a double check of upconversion effect. In the meantime, the OLED of most of the area was not working because of the degradation. After an extremely high bias of over $100V$ was applied, some dark pixels at the edge area started to work, although all were still very dim. This time the laser was turned off and moved to the new position where the pixels were working. The laser was still stuck at the back of the device, and when turning on the laser again, pixels with a round pattern became brighter at the corresponding position at the front of the device. However, soon they became dim and died. FIG. 4.4 shows the imaging results.

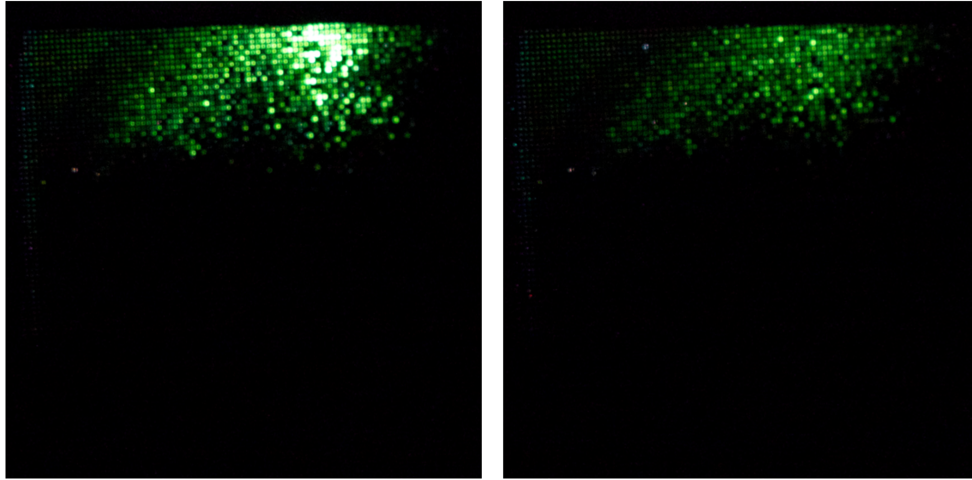

Figure 4.4: Imaging results when the mask was removed and the laser was directly placed at the back of device again (left), when the laser was turned off. The pixels get dim as the OLED was dying quickly.

4.4 Imaging result analysis

The pixellated infrared upconversion device successfully demonstrated the upconversion for light with a wavelength of $1.5\mu m$ to light with a wavelength of $520nm$. Although the projected infrared pattern of "IR" was not up-converted due to lack of a pixel-available working area and the weak optical power after light passed through the mask, one can still clearly see and recognize the light pattern when the laser was placed directly at the back of the imaging device, without the mask.

This infrared upconversion pixellated imaging device was made in a pixel array, of which each pixel's photodetector part was completely independent of others above the InP emitter layer. As for the continuous film of OLED, due to the extremely low mobility of holes in organic materials, the lateral diffusion of photon-induced carriers was neglected and the emitted light for the OLED was localized for each pixel. Therefore, the resolution

of this upconversion imaging device was very closely dependent on the size of each mesa. For each pixel, the spacing was 25 μm. The dimensions were fabricated as $70\mu m$ for both length and width, and the insulating window opened for the photocurrent flow through was 45 μm. The actual effective size counted for resolution should be the dimension of the mesa and the mesa spacing, for which the ideal resolution should be 95 μm. However, as illustrated in FIG. 4.3 and FIG. 4.4, the up-converted patterns for the laser did not show the exact rectangular shape of the laser beam, for several reasons: firstly, the laser beam was not collimated and expanded between the mask and the upconversion device, which caused the distortion and expansion of the beam pattern; secondly, the laser beam was not uniform so some corners of the pattern did not have enough optical power to trigger the OLED at the front of device, which resulted in a inconsistent shape of the brighter LED area; lastly, the dark current flowing through each pixel's HPT increased significantly after a certain level of bias as measured before. Therefore, when the device was under a bias of over $40V$, the dark current was already huge, which made the photocurrent less recognizable and hence blurred the pattern edge.

During the imaging test, the pixels at the center of device did not light up. The problem could have been due to either the OLED, the HPT, or the interfaces between the two parts. To examine where the problem rose, the imaging device was studied under a microscope. FIG. 4.5 is the microscopic picture of one corner of the imaging device. The pixel pointed at by the red arrow was the one not lit up, and the pixel pointed by the green arrow successfully lit up. The organic layers of the working pixels are all burned off due to the heat brought by the flowing current. However, the dark pixels have organic layers perfectly covered on top of it, which indicates that there was no current flowing through to the organic layers at that spot. Therefore, the OLED was not the part to blame for the non-working pixels.

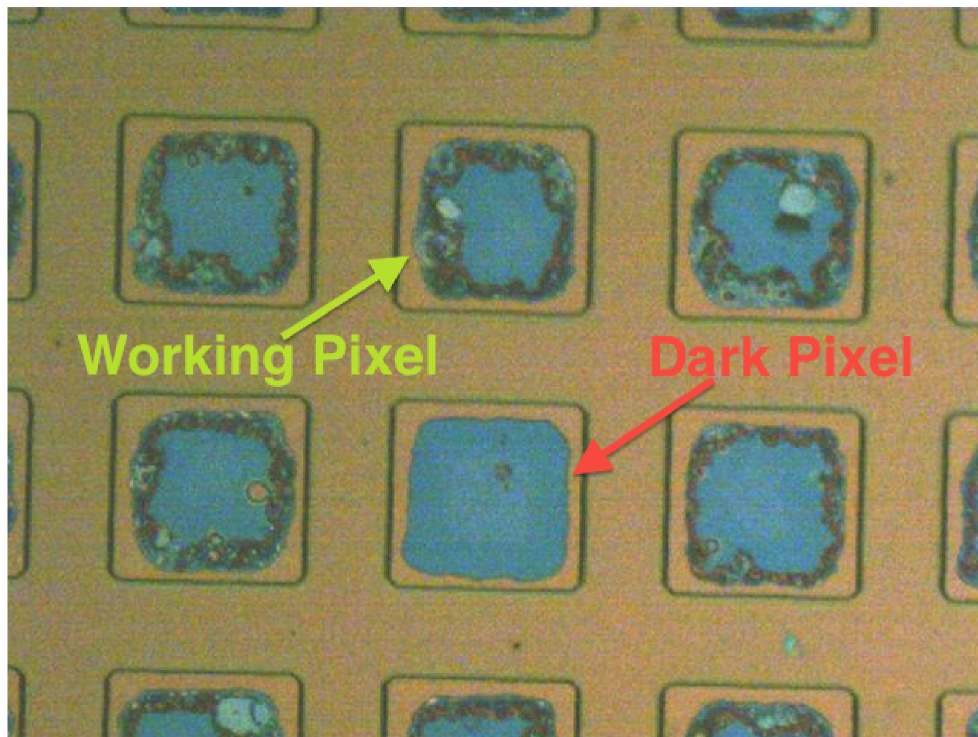

Figure 4.5: Pixels of the pixellated upconversion device after imaging test. The organic layers on the working pixel (yellow arrow) were burned off. The organic layers on the non-working pixel (red arrow) remained intact.

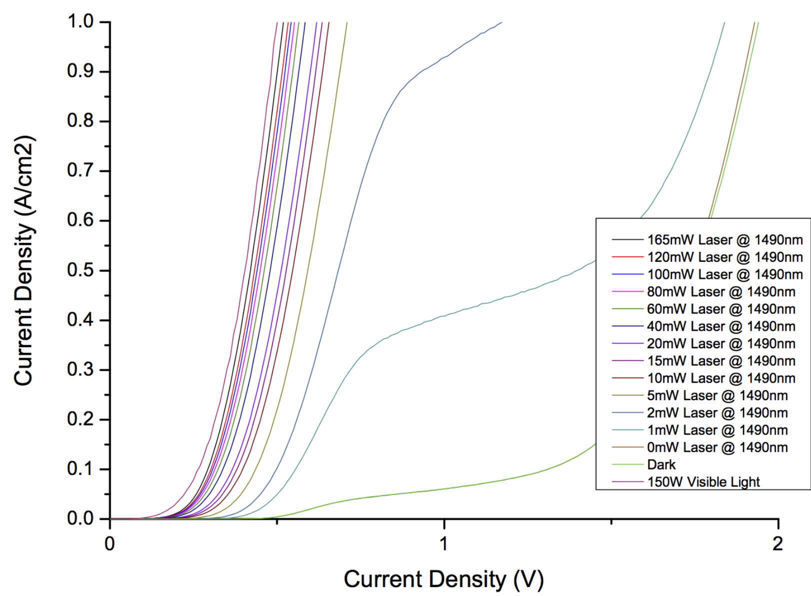

Figure 4.6: I-V curve of one pixel on the HPT mesa array under different levels of illumination power. The HPT mesa array and the pixellated were from the same wafer, and they were fabricated in one batch except the OLED deposition.

To further pinpoint the problem, one needs to find out whether it is the HPT or the interface causing the dark pixels. In addition, the upconversion imaging device, there was another dummy HPT mesa array that was taken from the same wafer as the imaging device and fabricated at the same time for all procedures except the OLED depositions. To diagnose the true reason for the malfunction of the dark pixels, we tested the HPT mesa array performances. Because both the imaging device and the HPT mesa array have the same structures, mesas of the HPT mesa array should perform the same as the mesas of the imaging device do. For an all-round test, several mesas at four corners and at the device center were chosen and measured for their I-V characteristics under various illumination powers. Due to the space constraints of the probe station, the infrared light was shone at the front rather than at the back of the device. All of the mesas tested worked properly, with the expected photo-responses. FIG. 4.6 is the I-V curve for one of the selected mesas. The dark current started to rise at 0.5V, and it gradually climbed up to a level below $0.1A/cm^2$. It then significantly increased when the bias was over 1.3V. Under different levels of infrared irradiation, the total currents all rose before 0.5V. For an input optical power of $1mW$, the total current density was measured to be $0.05A/cm^2$ at a bias of 0.5V, and it was pumped up to over $0.4A/cm^2$ with a bias of 1V. With an input optical power of 2mW, the output current density doubled to over $0.9A/cm^2$ with the same bias condition. When the input power was increased with the same power step differences, one can clearly observe the proportional increase of the total current from bias between $0.5A$ to $1.5A$, which was expected for a working HPT. There are over 10,000 pixels on the device; by selecting mesas from different areas of the device, our measurements showed that the photodetectors of the imaging device were working properly in most areas, although there may have been several non-working pixels on the device that were due to the non-uniformity caused by the complicated fabrication process. These were overlooked and not tested by coincidence.

Careful inspections of the imaging device confirm that the interface was the problem causing the dark pixels. The abnormal high voltage required to drive this upconverter and the fact that adding more bias could light up some pixels that were originally dark indicate that the electrical connection between the HPT and OLED was not uniform and good enough. Among the possible reasons are that the window opened in each mesa, which allowed contact with the OLED, still had a thin film of SiN in between, or that the surface of top-most HPT layers was oxidized. Both reasons may result in a higher resistance and required higher driving voltage. Another possibility could be the breaking of the cathode layers due to the uneven surface of the mesa array. Because the cathode layers were extremely thin (5nm for Al and 15 nm for Ag) and brittle, a very smooth surface was needed for safe deposition. However, the mesas had a height of $1.5\mu m$ with a spacing of $25\mu m$. The stepping of the mesa surface may have had just too large a slope for the cathode layers.

4.5 Challenges and future work

According to the results of this experiment, more studies are needed to be addressed the interfacial problems. When fabricating the next hybrid upconversion device, one needs to be extremely careful about the interfacial surface of the HPT mesas in order to avoid either the remaining insulating layer or oxidization during interfacial surface treatments. When cleaning the surface, UV-Ozone was usually used, which significantly oxidizes the InGaAs surface. Moreover, the dip in $(NH_4)_2S$ may not be helpful to completely etch off the oxidization layer. One should also try to optimize the mesa structure and lower the mesa height for more continuous and reliable cathode layer depositions. Once the interfacial problems have been solved, the pixellated device should have higher resolution as a result

of reduced mesas size and the spacing between them.

This pixellated device consists of a p-n-p HPT and an OLED. Although the p-n-p HPT has proved its advantages in amplifying the photocurrent, there is still room to improve. Due to the relatively lower mobility of holes, the p-n-p HPT does not perform as well as an n-p-n HPT to achieve a higher electrical gain and a faster response. In addition, during fabrication, it is usually more difficult to achieve a heavily doped p-type layer due to background n-type doping originating from the presence of impurities, vacancies, and interstitials, and due to the solubility of dopants. Therefore, using a n-p-n HPT instead of a p-n-p in our upconversion device, a higher gain as well as a higher responsivity for photo-detection are expected for the device's performance. The device should then be able to achieve an upconversion with higher sensitivity and overall efficiency. In the meantime, one should also pay extra attention to the dark current of HPT. The imaging results of the pixellated upconverter showed that pixels of the pixellated imaging upconverter were very bright when there was no infrared light shining at the device's back, which may lower the contrast between the up-converted infrared image and the background and may also result in a blurry and less sharp pattern edge for the up-converted pictures. To address this problem, one can moderately increase the width of the base layer of HPT. However, in doing so, a lower gain is expected.

As for the light emitting part, fluorescent OLED was used in this pixellated device and all previous hybrid upconverters. However, the fluorescent OLED has a maximum internal quantum efficiency of only 25%, which lowers the overall upconversion efficiency of the entire upconverter. To improve the overall upconversion efficiency, phosphorescent OLED is the better alternative because phosphorescent OLED can achieve 100% internal quantum efficiency, theoretically.

4.6 Conclusion

A pixellated hybrid infrared imaging upconverter has been designed, and has successfully demonstrated the upconversion of light from a wavelength of 1.5 μm to 520 nm. However, this pixellated imaging upconverter did not show the upconversion of an infrared letter pattern due to its short lifetime and few working pixels. The device was fabricated by depositing a thin film of fluorescent OLED on top of a 128 by 128 array of HPT mesas. The lateral carrier diffusion issue of previous upconversion devices was eliminated by the pixellated design, which allowed each photodetector to work independently, without affecting the others. Therefore, each pixel was able to maintain as high as an efficient single-element upconverter. A resolution of 95μm can be achieved, theoretically, based on the size of each pixel and the spacing between them. A higher resolution can be achieved by adjusting the pixel size. The results show that this infrared upconverter with its pixellated structure has great potential for high-resolution NIR imaging applications and can be combined with efficient single-element upconverter designs to achieve more sensitive infrared-image capturing.

Chapter 5

Summary and contributions

Infrared imaging technologies have attracted a lot of attentions due to its wide applications, and the imaging of infrared light at the eye-safe region ($1.5\mu m$) was of particular interest due to its various applications in military night visions, in industrial system maintenance, and in scientific deep space study. Therefore, the inorganic/organic hybrid upconversion imaging devices have been developed as an alternative of the current infrared imaging system with the advantage of possible higher efficiency and resolution. The hybrid imaging upconverters are targeted to convert infrared images of a NIR wavelength of $1.5\mu m$ to visible images. The thesis introduces works of both the hybrid pixel-less infrared imaging upconverter and the pixel-lated hybrid infrared imaging upconverter as follows:

The pixel-less Schottky-junction/OLED imaging upconversion device was designed, which integrated an $i - InGaAs/C_{60}$ hybrid Schottky junction and an OLED. The hybrid $InGaAs/C_{60}$ heterojunction exhibited a photovoltaic effect through its photoresponse with infrared light and the light intensity dependency of its photocurrent. The generated photocurrent was then injected to the OLED emissive layer to emit the green light. The

particular structure of this device also had its interconnection region of photodetector and OLED completely depleted under bias, resulting in a suppression of the lateral carrier diffusion yet maintaining a effective electrical connection of the photodetector and the OLED. The hybrid pixel-less infrared imaging device successfully up-converted an infrared letter pattern to a recognizable visible image with a spatial resolution of 10 mum, which demonstrated the first-ever inorganic/organic hybrid pixelless imaging.

The pixel-lated HPT/OLED imaging upconversion device was designed with a 128 by 128 InGaAs HPT mesa array, on which a thin continuous film of OLED was deposited. Single-element devices with similar structures proved to have achieved very high overall upconversion efficiencies. The HPT functioned as photodetector, and in the meantime, it amplified the photocurrent before the current was injected to the OLED. The photodetector array consisted separate HPT mesas with a size of $70\mu m$ and the spacing of them was $25\mu m$. Because each mesa worked individually, therefore the pixel-lated device had no issue of photo-induced carrier lateral spreading, and it can give a spatial resolution of $95\mu m$, theoretically. The hybrid pixel-lated infrared imaging device successfully showed an upconversion for light with a wavelength of $1.5\mu m$ to $520nm$, and it was the first-ever upconversion demonstration for the pixel-lated upconverter.

References

[1] "Infrared study press release". http://www.flowresearch.com/Press_Releases/Website/InfraredStudyRelease.htm. Accessed: 30/09/2012.

[2] Hany Aziz, Yichun Luo, Gu Xu, and Zoran D. Popovic. "Improving the stability of organic light-emitting devices by using a thin mg anode buffer layer". *Applied Physics Letters*, 89(10):103515, 2006.

[3] Hany Aziz, Zoran D. Popovic, Nan-Xing Hu, Ah-Mee Hor, and Gu Xu. "Degradation mechanism of small molecule-based organic light-emitting devices". *Science*, 283(5409):1900–1902, 1999.

[4] I. Baker and C. Maxey. "Summary of HgCdTe 2D array technology in the u.k.". *Journal of Electronic Materials*, 30:682–689, 2001. 10.1007/BF02665856.

[5] D Ban, S Han, Z. H Lu, T Oogarah, A. J Springthorpe, and H. C Liu. "Near-infrared to visible light optical upconversion by direct tandem integration of organic light-emitting diode and inorganic photodetector". *Applied Physics Letters*, 90(9):3108–3110, February 2007.

[6] D Ban, H Luo, H. C Liu, Z. R Wasilewski, Y Paltiel, A Raizman, and A Sher. "Midinfrared optical upconverter". *Applied Physics Letters*, 86(20), May 2005.

[7] D Ban, H Luo, H. C Liu, Z. R Wasilewski, A. J Springthorpe, R Glew, and M Buchanan. "Optimized GaAs/AlGaAs light-emitting diodes and high efficiency wafer-fused optical up-conversion devices". *Journal of Applied Physics*, 96(9):5243–5248, November 2004.

[8] D Ban, H Luo, HC Liu, AJ SpringThorpe, R Glew, ZR Wasilewski, and M Buchanan. "1.5 to 0.87 μm optical upconversion device fabricated by wafer fusion". *Electronics Letters*, 39(15):1145–1147, July 2003.

[9] D. Ban, Hui Luo, H.C. Liu, Z.R. Wasilewski, and M. Buchanan. "Pixelless $1.5 - \mu m$ up-conversion imaging device fabricated by wafer fusion". *IEEE Photonics Technology Letters*, 17(7):1477–1479, July 2005.

[10] Dayan Ban, Jun Chen, Michael G. Helander, Zhenghong Lu, Marcel Graf, Anthony J. SpringThorpe, P. Poole, and H. C. Liu. "Infrared organic/inorganic optical upconverting devices". *Proceedings of SPIE*, 2009.

[11] Dayan Ban, S. Han, Z. H. Lu, T. Oogarah, A. J. SpringThorpe, and H. C. Liu. "Organic-inorganic hybrid optical upconverter". *IEEE Transactions on Electron Devices*, 54(7):1645–1650, July 2007.

[12] A Boucherif, D Ban, H Luo, E Dupont, Z Wasilewski, H Liu, Y Paltiel, A Raizman, and A Sher. "InAsSb based mid-infrared optical upconversion devices operable at thermoelectric temperatures". *Electronics Letters*, 44(4):312–313, February 2008.

[13] Liann-Be Chang, Ching-Chuan Shiue, and Ming-Jer Jeng. "High reflective p-GaN/Ni/Ag/Ti/Au Ohmic contacts for flip-chip light-emitting diode (FCLED) applications". *Applied Surface Science*, 255(12):6155 – 6158, 2009.

[14] J Chen, D Ban, MG Helander, Z Lu, M Graf, P Poole, and HC Liu. "Near-infrared optical upconverter with integrated heterojunction phototransistor and organic light-emitting diode". *IEEE Photonics Technology Letters*, 21(19):1447–1449, October 2009.

[15] J Chen, D Ban, MG Helander, Z Lu, M Graf, AJ SpringThorpe, and HC Liu. "Near-infrared optical upconverter based on $i-In_{0.53}Ga_{0.47}As/C_{60}$ photovoltaic heterojunction". *Electronics Letters*, 45(14):753–755, July 2009.

[16] Jun Chen. *"Hybrid organic/inorganic optical upconversion devices"*. PhD thesis, University of Waterloo, 2011.

[17] Jun Chen, Dayan Ban, Xiaodong Feng, Zhenghong Lu, Saeed Fathololoumi, Anthony J Springthorpe, and H. C Liu. "Enhanced efficiency in near-infrared inorganic/organic hybrid optical upconverter with an embedded mirror". *Journal of Applied Physics*, 103(10):3112–3116, May 2008.

[18] Jun Chen, Dayan Ban, Xiaodong Feng, Zhenghong Lu, Saeed Fathololoumi, Anthony J. Spring Thorpe, and H. C Liu. "Near-infrared inorganic/organic hybrid optical upconverter with an embedded mirror". *Phys. Status Solidi (c)*, 6(S1):23–26, April 2009.

[19] Jun Chen, Dayan Ban, Michael G Helander, Zheng-Hong Lu, and Philip Poole. "Near-infrared inorganic/organic optical upconverter with an external power efficiency of >100%". *Advanced Materials*, 22(43):4900–4904, August 2010.

[20] Jun Chen, Jianchen Tao, Dayan Ban, Michael G. Helander, Zhibin Wang, Jacky Qiu, and Zhenghong Lu. "Hybrid organic/inorganic optical up-converter for pixel-less near-infrared imaging". *Advanced Materials*, 24(23):3138–3142, 2012.

[21] Masayuki Chikamatsu, Yoshiro Ichino, Noriyuki Takada, Manabu Yoshida, Toshihide Kamata, and Kiyoshi Yase. "Light up-conversion from near-infrared to blue using a photoresponsive organic light-emitting device". *Applied Physics Letters*, 81(4):769–771, 2002.

[22] E Dupont and S Chiu. "Efficient light emitting diodes by photon recycling and their application in pixelless infrared imaging devices". *Journal of Applied Physics*, 87(3):1023–1028, February 2000.

[23] M. Dutta and M. A. Stroscio. *"Advanced semiconductor heterostructures"*. World Scientific Publishing, 2003.

[24] Xiaodong Feng. *"Development of 8-Hydroxyquinoline metal based organic-light emitting diodes"*. PhD thesis, University of Toronto, 2008.

[25] G.D.Henshall, P.D.Greene, W.O.Bourne, D.R.P.Guy, D.D.Besgrove, N.Apsley, L.L.Taylor, and S.J.Bass. "A 5 $\times$ 5 monolithic ingaas/inp multiple quantum well spatial light modulator array". 1990.

[26] G.D.Zhou. *"Fundamentals of Structural Chemistry"*. World Scientific, 1993.

[27] Brian A. Gregg and Mark C. Hanna. "Comparing organic to inorganic photovoltaic cells: theory, experiment, and simulation". *Journal of Applied Physics*, 93(6):3605–3614, 2003.

[28] R. N. Hall. "Electron-Hole recombination in germanium". *Physical Review*, 87(2):387, July 1952.

[29] H.C.Liu, Jianmeng Li, Z.R.Wasilewski, and M.Buchan. "Integrated quantum well intersubband photodetector and light-emitting diode for thermal imaging". *SPIE*, 2552:336–342, January 1995.

[30] Wendy U. Huynh, Janke J. Dittmer, and A. Paul Alivisatos. "Hybrid nanorod-polymer solar cells". *Science*, 295(5564):2425–2427, 2002.

[31] Do Young Kim, Kaushik Roy Choudhury, Jae Woong Lee, Dong Woo Song, Galileo Sarasqueta, and Franky So. "PbSe nanocrystal-based infrared-to-visible up-conversion device". *Nano Letters*, 11(5):2109–2113, 2011.

[32] Do Young Kim, Dong Woo Song, Neetu Chopra, Pieter De Somer, and Franky So. "Organic infrared upconversion device". *Advanced Materials*, 22(20):2260–2263, 2010.

[33] D.Y Kim, D.W Song, N Chopra, P De Somer, and F So. "Organic infrared upconversion device". *Advanced Materials*, 22(20):2260–2263, March 2010.

[34] Hyo-Chang Kim, Jorg Wiedmann, Kensuke Matsui, Shigeo Tamura, and Shigehisa Arai. "1.5 μm-wavelength distributed feedback lasers with deeply etched first-order vertical grating". *Japanese Journal of Applied Physics*, 40:1107, 2001.

[35] Nobuaki Kojima, Masafumi Yamaguchi, and Naomi Ishikawa. "Analysis of photovoltaic properties of C_{60}-Si heterojunction solar cells". *Japanese Journal of Applied Physics*, 39(Part 1, No. 3A):1176–1179, 2000.

[36] Makoto Konagai, Kosho Katsukawa, and Kiyoshi Takahashi. "(GaAl)As/GaAs heterojunction phototransistors with high current gain". *Journal of Applied Physics*, 48(10):4389–4394, 1977.

[37] R. Könenkamp, G. Priebe, and B. Pietzak. "Carrier mobilities and influence of oxygen in C_{60} films". *Phys. Rev. B*, 60:11804–11808, Oct 1999.

[38] PW Kruse, FC Pribble, and RG Schulze. "Solid-state infrared-wavelength converter employing high quantum efficiency Ge/GaAs heterojunction". *Journal of Applied Physics*, 38(4):1718–1720, March 1967.

[39] LY Leu, JT Gardner, and SR Forrest. "A high-gain, high-bandwidth $In_{0,53}Ga_{0,47}As/lnP$ heterojunction phototransistor for optical communications". *Journal of Applied Physics*, 69(2):1052–1062, January 1991.

[40] B. F. Levine. "Quantum-well infrared photodetectors". *Journal of Applied Physics*, 74(8):R1, 1993.

[41] H. C. Liu, H. Luo, D. Ban, M. Buchanan, Z. R. Wasilewski, A. J. SpringThorpe, and P. J. Poole. "Photon upconversion devices for imaging". pages 698431–698431–7, 2008.

[42] H.C. Liu, L.B. Allard, M. Buchanan, and Z.R. Wasilewski. "Pixelless infrared-imaging device". *Electronics Letters*, 33(5):379–380, February 1997.

[43] H.C. Liu, M. Gao, and P.J. Poole. "1.5 μm up-conversion device". *Electronics Letters*, 36(15):1300–1301, July 2000.

[44] L.M. Lunardi, S. Chandrasekhar, and R.A. Hamm. "High-speed, high-current-gain p-n-p InP/InGaAs heterojunction bipolar transistors". *Electron Device Letters, IEEE*, 14:19–21, 1993.

[45] H Luo, D Ban, H. C Liu, Z. R Wasilewski, and M Buchanan. "Optical upconverter with integrated heterojunction phototransistor and light-emitting diode". *Applied Physics Letters*, 88(7), February 2006.

[46] H. Luo, D. Ban, H.C. Liu, P.J. Poole, and M. Buchanan. "Pixelless imaging device using optical up-converter". *IEEE Electron Device Letters*, 25(3):129–131, March 2004.

[47] H Luo, D Ban, HC Liu, AJ SpringThorpe, ZR Wasilewski, M Buchanan, and R Glew. "1.5 μm to 0.87 μm optical upconversion using wafer fusion technology". *Journal of Vacuum Science and Technology A: Vacuum, Surfaces, and Films*, 22(3):788–791, May 2004.

[48] T. Moriizumi and K. Takahashi. "Theoretical analysis of heterojunction phototransistors". *Electron Devices, IEEE Transactions on*, 19(2):152 – 159, feb 1972.

[49] M.Pope and C.E.Swenberg. *"Electronic Processes in Organic Crystals and Polymer"*. Oxford University Press, 2 edition, 1999.

[50] Jingping Ni, Takanori Tano, Yoshiro Ichino, Takeshi Hanada, Toshihide Kamata, Noriyuki Takada, and Kiyoshi Yase. "Organic light-emitting diode with tiopc layer—a new multifunctional optoelectronic device". *Japanese Journal of Applied Physics*, 40(Part 2, No. 9A/B):L948–L951, 2001.

[51] Masato Ofuji, Ken Ishikawa, Hideo Takezoe, Katsuhiko Inaba, and Kazuhiko Omote. "Crystallite size effect on the hole mobility of uniaxially aligned copper phthalocyanine thin-film field-effect transistors". *Applied Physics Letters*, 86(6):062114, 2005.

[52] Peter Peumans, Soichi Uchida, and Stephen R. Forrest. "Efficient bulk heterojunction photovoltaic cells using small-molecular-weight organic thin films". 425:158–162, 2003.

[53] J. Piotrowski and W. Gawron. "Ultimate performance of infrared photodetectors and figure of merit of detector material". *Infrared Physics & Technology*, 38(2):63 – 68, 1997.

[54] M. Pope, H. P. Kallmann, and P. Magnante. "Electroluminescence in organic crystals". *The Journal of Chemical Physics*, 38(8):2042–2043, 1963.

[55] Tobias Rauch, Michaela Boberl, Sandro F. Tedde, Jens Furst, Maksym V. Kovalenko, Gunter Hesser, Uli Lemmer, Wolfgang Heiss, and Oliver Hayden. "Near-infrared imaging with quantum-dot-sensitized organic photodiodes". *Nature Photonics*, 3:332–336, 2009.

[56] A. Rogalski. "Quantum well photoconductors in infrared detector technology". *Journal of Applied Physics*, 93(8):4355–4391, 2003.

[57] K Russell, Ian Appelbaum, H Temkin, C Perry, V Narayanamurti, M Hanson, and A Gossard. "Room-temperature electro-optic up-conversion via internal photoemission". *Applied Physics Letters*, 82(18):2960–2962, May 2003.

[58] W. Shockley W. Shockley. "Auger recombination in semiconductor quantum wells". *Physical Review B*, 58(7):4039, 1998.

[59] S. A. Van Slyke, C. H. Chen, and C. W. Tang. "Organic electroluminescent devices with improved stability". *Applied Physics Letters*, 69(15):2160–2162, 1996.

[60] S.M.Sze. *"Physics of semiconductor devices"*. 1981.

[61] C. W. Tang and S. A. VanSlyke. "Organic electroluminescent diodes". *Applied Physics Letters*, 51(12):913–915, 1987.

[62] K. Y. F Tsai, M. G Helander, and Z. H Lu. "Interfacial electronic structure of a hybrid organic-inorganic optical upconverter device: The role of interface states". *Journal of Applied Physics*, 105(8):3706–3712, April 2009.

[63] Bryan M van der Ende, Linda Aarts, and Andries Meijerink. "Lanthanide ions as spectral converters for solar cells". *Physical Chemistry Chemical Physics*, 11(47):11081–11095, September 2009.

[64] Danny Vennerberg and Zhiqun Lin. "Upconversion nanocrystals: Synthesis, properties, assembly and applications". *Science of Advanced Materials*, 3(1):26–40, 2011.

[65] Lian Wang, Myung-Han Yoon, Gang Lu, Yu Yang, Antonio Facchetti, and Tobin J. Marks. "High-performance transparent inorganic-organic hybrid thin-film n-type transistors". *Nature Materials*, 5:893–900, 2006.